Check for updates

Experimental study of the proton-transfer reaction C + H$_2^+$ → CH$^+$ + H and its isotopic variant (D$_2^+$)

Pierre-Michel Hillenbrand, [iD] *[ab] Kyle P. Bowen,[a] Fabrice Dayou,[c] Kenneth A. Miller,[a] Nathalie de Ruette,†[a] Xavier Urbain [iD] [d] and Daniel W. Savin*[a]

We report absolute integral cross section (ICS) measurements using a dual-source merged-fast-beams apparatus to study the titular reactions over the relative translational energy range of $E_r \sim$ 0.01–10 eV. We used photodetachment of C$^-$ to produce a pure beam of atomic C in the ground electronic ^{3}P term, with statistically populated fine-structure levels. The H$_2^+$ and D$_2^+$ were formed in an electron impact ionization source, with well known vibrational and rotational distributions. The experimental work is complemented by a theoretical study of the CH$_2^+$ electronic system in the reactant and product channels, which helps to clarify the possible reaction mechanisms underlying the ICS measurements. Our measurements provide evidence that the reactions are barrierless and exoergic. They also indicate the apparent absence of an intermolecular isotope effect, to within the total experimental uncertainties. Capture models, taking into account either the charge-induced dipole interaction potential or the combined charge-quadrupole and charge-induced dipole interaction potentials, produce reaction cross sections that lie a factor of ∼4 above the experimental results. Based on our theoretical study, we hypothesize that the reaction is most likely to proceed adiabatically through the 1^4A′ and 1^4A″ states of CH$_2^+$ *via* the reaction C(^{3}P) + H$_2^+$($^2\Sigma_g^+$) → CH$^+$($^3\Pi$) + H(^{2}S). We also hypothesize that at low collision energies only H$_2^+$($v \leq$ 2) and D$_2^+$($v \leq$ 3) contribute to the titular reactions, due to the onset of dissociative charge transfer for higher vibrational v levels. Incorporating these assumptions into the capture models brings them into better agreement with the experimental results. Still, for energies ≲0.1 eV where capture models are most relevant, the modified charge-induced dipole model yields reaction cross sections with an incorrect energy dependence and lying ∼10% below the experimental results. The capture cross section obtained from the combined charge-quadrupole and charge-induced dipole model better matches the measured energy dependence but lies ∼30–50% above the experimental results. These findings provide important guidance for future quasiclassical trajectory and quantum mechanical treatments of this reaction.

1 Introduction

Binary ion–molecule reactions are a fundamental class of gas-phase chemical reactions. Such processes also feature prominently in numerous chemical situations, including astrochemistry,[1,2] combustion,[3,4] fusion plasmas,[5] planetary atmospheres,[6–8] and plasma processing.[9,10] Studies of these

and other chemistries require reliable reaction dynamics data (*i.e.*, cross sections, such as we report here) and kinetics data (*i.e.*, rate coefficients, which can be generated from dynamics studies). Much of the required data come from laboratory measurements,[11] but experimental limitations hinder laboratory studies for many systems and reactions. Theory can be used to fill these gaps, but theoretical and computational challenges require using approximations to enable tractable calculations.

Quantum mechanical (QM) treatments of the dynamics of ion–molecule reactions are limited by numerous challenges.[12–14] Three-atom reaction systems represent the state of the art, but even there the various QM methods have yet to converge.[15–19] Four-atom systems are just beyond current QM capabilities.[14,20,21] Due to these limitations, the vast majority of theoretical dynamics

[a] *Columbia Astrophysics Laboratory, Columbia University, New York, NY 10027, USA. E-mail: p.m.hillenbrand@gsi.de, dws26@columbia.edu*
[b] *Institut für Kernphysik, Goethe-Universität, 60438 Frankfurt, Germany*
[c] *Sorbonne Université, Observatoire de Paris, PSL University, CNRS, LERMA, F-92195 Meudon, France*
[d] *Institute of Condensed Matter and Nanosciences, Université catholique de Louvain, B-1348 Louvain-la-Neuve, Belgium*
† Present address: European Spallation Source ERIC, SE-22100 Lund, Sweden.

data have been determined using either the quasi-classical trajectory (QCT) method,[22] phase space theory,[23,24] or a variety of capture models,[25,26] among them the widely used Langevin–Gioumousis–Stevenson (LGS) model.[24,27] Laboratory measurements are needed to benchmark these theoretical studies to guide their continued development.

Our work here focuses specifically on reaction dynamics, namely translational-energy-dependent studies. These provide the most sensitive probes of the underlying quantum mechanics of chemical reactions. These studies can, in turn, be integrated over energy to generate temperature-dependent reaction kinetics. Such results are important to test theoretical methods that are only capable of generating kinetics data, such as transition state theory[28] or the more recent ring polymer molecular dynamics[29] approach. Similarly, many experimental methods can only generate kinetics data. As reviewed elsewhere,[11] some of these laboratory techniques include selected ion flow drift tube, selected ion flow tube, cinétique de réactions en écoulement supersonique uniforme (CRESU), flowing afterglow, ion cyclotron resonance mass spectrometry, and flow-drift tube. These techniques use pseudo-first-order methods to measure thermal rate coefficients. But the methods are not capable of measuring the magnitude nor energy dependence of the underlying dynamics that produces the kinetics. All together, while these theoretical and experimental kinetics data are important for chemical models, they are not a sensitive probe of the dynamics of the reactions.

The simplest ion–molecule reaction involving three-atom systems is proton transfer, and the simplest H-bearing diatomic cation is H_2^+. For these reasons, reactions involving H_2^+ and its isotopic variants undergoing proton transfer with neutral atoms have been the focus for numerous QM and QCT dynamics investigations. Over the past five or so years, theoretical studies have been performed for reactions with He,[30–32] Li,[33,34] O,[16–19] Ne,[35–38] and Ar.[39] Earlier works can be found in the bibliographies of the cited references. We are unaware of any QM or QCT studies for proton-transfer reactions involving H_2^+ isotopologues with other neutral atoms. Going back to the 1970s and 1980s, Gentry and his collaborators carried out a series of experimental and theoretical studies for D_2^+ reacting with C,[40] N,[41,42] O,[43] and F[44] atoms. In each case an LGS-type capture model, which included several contributions to the long-range interactions, was employed to compute the reaction cross section.[45]

Absolute cross section measurements of proton transfer for three-atom systems are of critical importance for advancing our theoretical understanding of the field, a necessary step before the community can successfully move on to four-or-more-atom systems. Numerous groups have reported experimental dynamics results for H_2^+ reacting with He and Ne. Brief reviews can be found in two recent laboratory studies.[46,47] Absolute integral cross section (ICS) measurements for these neutrals have been performed using crossed-beams,[48] merged-beams,[49] and guided ion beam (GIB)[46,47,50–52] methods.

The H_2^+ beams for the crossed-beams and merged-beams studies were produced using electron-impact-ionization (EII)

ion sources, which generate ions that are rotationally and vibrationally excited. The GIB studies use laser techniques, such as vacuum ultraviolet photoexcitation followed by pulsed field ionization, to prepare rovibrational-state-selected H_2^+, which generates low ion beam currents.

For the neutral atom reagent, the crossed-beams study[48] used an effusive gas source, essentially limiting this approach to reactions with stable gases. The merged-beams study[49] used charge transfer to generate the neutral beam. This approach starts with ions from a second EII source, the beam of which was then passed through a gas cell where a fraction of the ions undergo charge transfer (CT) to create a neutral atom beam by then electrostatically or magnetostatically removing any remaining ions. This approach enables one to study reactions with transient neutral atoms and was used by Gentry and his co-workers for their studies of D_2^+ reacting with C,[40] N,[41,42] O,[43] and F.[44] But the charge-transfer approach can generate unknown fractions of neutral atoms in metastable terms, complicating the interpretation of the results (as we discuss below). Lastly, the low ion currents of the rovibrational-state-selection method require using gas-cell targets to yield measurable signal rates for dynamics studies. This necessitates the use of stable target gases such as He,[46] Ne,[47] and Ar,[53] the latter of which was performed with state-selected O_2^+. But the approach has also enabled absolute dynamics studies for four-or-more-atom systems involving various state-selected molecular ions reacting with stable gases such as H_2,[54] HD,[55] D_2,[54] CO,[56] N_2,[57] H_2O,[57] CH_4,[58] and C_2H_4.[59]

Here we present experimental results using a merged-beams approach that enables us to perform absolute measurements for proton-transfer involving isotopologues of H_2^+ with a known rovibrational distribution reacting with transient neutral atoms in their ground electronic term. The H_2^+ ions are produced in an EII discharge source, which generates H_2^+ and D_2^+ with well known vibrational and rotational distributions.[60–64] Photodetachment of an atomic anion beam is used to produce the ground-term neutral atoms. This approach thus enables absolute ICS measurements for reactions involving two well characterized transient species and enables us to study reaction systems that are not accessible using the rovibrational-state-selected method, which is best suited for studies involving one transient and one stable species.

More specifically, we present absolute ICS measurements for the proton-transfer reaction

$$C(^3P) + H_2^+(^2\Sigma_g^+) \rightarrow CH^+ + H, \qquad (1)$$

and its isotopic variant, the deuteron-transfer reaction

$$C(^3P) + D_2^+(^2\Sigma_g^+) \rightarrow CD^+ + D. \qquad (2)$$

The measurements were performed for relative kinetic energies from 0.007 to 6.3 eV for reaction (1), and from 0.013 to 8.7 eV for reaction (2).

As mentioned earlier, reaction (2) has previously been studied experimentally by Gentry and his collaborators.[40,45] For their measurements, they started with C^+ with unknown fractions of ground (^2S) and metastable (^4P) ions. CT was used

This journal is © the Owner Societies 2020

Phys. Chem. Chem. Phys., 2020, **22**, 27364–27384 | **27365**

to form the C beam, but with unknown fractions of ground (^{3}P) and metastable (^{1}D, ^{1}S, and ^{5}S) atoms. As a result, there were four different possible levels of internal excitation and three different possible spin multiplicities in their C beam. It is unlikely that these levels and multiplicities all contributed equally (or at all) to the formation of the measured CD$^+$. These uncertainties hinder a proper comparison with theoretical approaches.

One of the aims of our work is to perform similar measurements but with a pure beam of ground-term atomic C, thereby providing more reliable experimental benchmarks for theory. Additionally, our use of H$_2^+$ and D$_2^+$ allows us to quantify the effects of isotopic substitution on reactivity. The experimental work is complemented by a theoretical study of the reactant and product channels of the CH$_2^+$ system, which helps to clarify the possible reaction mechanisms underlying the ICS measurements.

The rest of the paper is organized as follows: Section 2 describes our experimental method. Section 3 is a theoretical study of the reactant and product channels. Section 4 presents our experimental results, while Section 5 discusses them in more detail. Lastly, Section 6 summarizes our findings.

2 Experiment

The experimental apparatus and methodology have been described in detail elsewhere.[14,20,21,65] Below, we only briefly review those aspects of the apparatus and methodology that are new or specific to our measurements of reactions (1) and (2).

Our measurements were performed using a dual-source, merged-fast-beams apparatus. With this approach, we can carry out absolute ICS measurements of the dynamics for reactive scattering involving neutral atoms and molecular cations. We measured the charged products of the reaction.

More specifically, we measured the merged-beams rate coefficient $\langle\sigma v_r\rangle$, where σ is the reaction ICS, v_r is the relative velocity, and the brackets signify an averaging over the energy spread of the experiment. The data were collected *versus* the relative translational energy E_r. One advantage of the merged-beams rate coefficient is that the trivial v_r^{-1} dependence of σ is removed from the results. This enables us to explore for any isotope effect in the kinetics of the reactive scattering process, due to the different reduced mass for each collision system, which is given by

$$\mu = \frac{m_n m_i}{m_n + m_i}. \quad (3)$$

Here m_n and m_i are the masses of the neutral atom and cation molecule, respectively. We can also express our experimental results as $\langle\sigma E_r^{1/2}\rangle = (\mu/2)^{1/2}\langle\sigma v_r\rangle$. This removes both the trivial v_r^{-1} dependence in σ and that of the reduced mass, and enables us to study the subtleties in the dynamics of the reactive scattering.[24,27] The ICS was extracted from the data using the known energy spread of the experiment.

2.1 Cation beam

Cations were formed using a duoplasmatron (an EII source), electrostatically extracted and accelerated, and mass-to-charge

selected to form the desired ion beam. The ion source operating parameters were adjusted to maximize the production of diatomic cations by working with a low electron beam current and at low gas pressure, with both still being sufficient to maintain the discharge. The gas pressure measured just outside the source was $\sim 4.8 \times 10^{-6}$ Torr, using a vacuum gauge calibrated for H$_2$. This corresponds to a pressure inside the source of ~ 0.048 Torr.[21] These parameters resulted in essentially pure beams of H$_2^+$ and D$_2^+$, as described below. The laboratory translational energy of the H$_2^+$ beam was $E_{H_2^+} = 4.66$ keV and that of the D$_2^+$ beam was $E_{D_2^+} = 9.40$ keV. With masses of 2.01533 and 4.02765 u, these correspond to translational energies of 2.31 and 2.33 keV u^{-1}, respectively.

The cation beam was collimated using a pair of 5 mm apertures before being electrostatically deflected and merged onto the neutral beam. We used a Faraday cup before this beam merger to measure the cation current entering the interaction region.

2.2 Cation beam purity

We used a gas of H$_2$ to generate H$_2^+$ ($m_i/q = 2$) and of D$_2$ to generate D$_2^+$ ($m_i/q = 4$), where q is the charge of the cation. Over the years, we have used both H$_2$ and D$_2$ separately and together in our duoplasmatron. We verified that there was insignificant cross contamination in the source that could lead to D$^+$ in our $m_i/q = 2$ beam and H$_2$D$^+$ in our $m_i/q = 4$ beam. Mass scans performed when using H$_2$ showed no signs of D$_2^+$, indicating that there was no D$_2$ present in the source and hence no D$^+$ contamination of our H$_2^+$ beam.

Mass scans performed when using D$_2$ in the source showed a small level of H contamination in the plasma discharge, possibly due to water vapor in the gas line or the ion source. In order to quantify the fraction of H$_2$D$^+$ contamination in the $m_i/q = 4$ beam, we measured the CH$^+$ signal from the reaction

$$C + H_2D^+ \rightarrow CH^+ + HD. \quad (4)$$
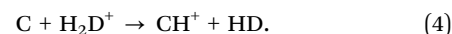
Using the final analyzer of the apparatus, this signal is readily distinguishable from the CD$^+$ signal of reaction (2). For matched C and $m_i/q = 4$ beam velocities (corresponding to $E_r = 13 \pm 9$ meV, as discussed below), the measured CH$^+$ signal rate for reaction (4) was $S = 0.0118 \pm 0.0125$ s^{-1}. Here and throughout, all uncertainties are given at an estimated one-sigma statistical confidence level. This signal rate is consistent with zero contamination. Additionally, we have previously measured the CH$^+$ signal for the isotopic variant of reaction (4), namely,[14]

$$C + H_3^+ \rightarrow CH^+ + H_2. \quad (5)$$
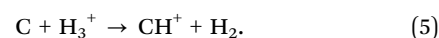
This enabled us to further quantify the H$_2$D$^+$ contamination from the cross section measured using the above given signal rate (and corresponding experimental parameters described below) and comparing it to the cross section for reaction (4), which we estimated to be 2/3rds of that for reaction (5) due to the reduced number of H nuclei available for transfer. From this, we inferred an H$_2$D$^+$ contamination of $0.34 \pm 0.36\%$, indicating that our $m_i/q = 4$ beam was essentially pure D$_2^+$.

27366 | *Phys. Chem. Chem. Phys.*, 2020, **22**, 27364–27384

This journal is © the Owner Societies 2020

2.3 Cation beam vibrational and rotational distributions

The population distributions over the vibrational v and rotational j states of H_2^+ and D_2^+ formed in EII sources are well known from theoretical and experimental studies.[60–64] The vibrational distribution, $p_{vib}(v)$, and rotational distribution, $p_{rot}(j)$, are essentially independent. Furthermore, j does not change significantly during the ionization process in and extraction from the source plasma. Additionally, the rovibrational levels of H_2^+ and D_2^+ have lifetimes on the order of 10^7 s. Hence, the rovibrational populations change insignificantly during the ~ 10 μs flight time to the interaction region.

It has been found experimentally that the neutral molecules in an EII source are in thermal equilibrium with a gas kinetic temperature of ≈ 400–500 K.[61,64] At such temperatures the neutrals are almost exclusively in the lowest vibrational level ($v' = 0$) of their ground electronic state. Thus, H_2^+ and D_2^+ form in an EII source *via* the ionization processes

$$H_2(v' = 0, j) + e^- \rightarrow H_2^+(v, j) + 2e^- \qquad (6)$$

$$D_2(v' = 0, j) + e^- \rightarrow D_2^+(v, j) + 2e^- \qquad (7)$$
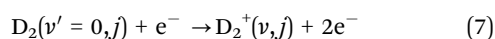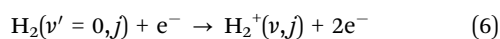
The resulting vibrational population distribution $p_{vib}(v)$ was first studied experimentally and theoretically by von Busch and Dunn, who derived an effective matrix element for ionization that depends on the internuclear distance.[60] Their results have been confirmed experimentally by several different groups.[61–64] The corresponding values for $p_{vib}(v)$ are given in Table 1.

The rotational population distribution $p_{rot}(j)$ arises from the thermal equilibrium achieved in the source plasma for the neutral molecules. The distribution depends on the temperature as[61]

$$p_{rot}(j) = \frac{g_I(2j+1)\exp\left[\dfrac{-B_e\, j(j+1)}{k_B T}\right]}{\displaystyle\sum_{j=0}^{\infty} g_I(2j+1)\exp\left[\dfrac{-B_e\, j(j+1)}{k_B T}\right]}, \qquad (8)$$

where g_I is the nuclear spin degeneracy factor, B_e is the rotational constant of the neutral molecule, and T is the gas temperature. Applying the selection rules according to the symmetrization postulate,[66] g_I for H_2 is

$$g_I = \begin{cases} 1 & \text{if } j \text{ even} \\ 3 & \text{if } j \text{ odd,} \end{cases}$$

and for D_2 it is

$$g_I = \begin{cases} 6 & \text{if } j \text{ even} \\ 3 & \text{if } j \text{ odd,} \end{cases}$$

The value of B_e is 60.853 cm^{-1} and 30.443 cm^{-1} for H_2 and D_2, respectively.[67] Lastly, extensive photodissociation measurements performed with a duoplasmatron source identical to the one employed here have infered that $T \approx 500$ K.[64] We used this value of T to calculate the rotational distribution $p_{rot}(j)$ given in Table 1.

Table 1 H_2^+ and D_2^+ vibrational population distribution $p_{vib}(v)$, from von Busch and Dunn,[60] and rotational population distribution $p_{rot}(j)$, from eqn (8), arising from the EII source. The sum of each distribution is normalized to unity

	$p_{vib}(v)$			$p_{rot}(j)$	
v	H_2^+	D_2^+	j	H_2^+	D_2^+
0	0.11916	0.04478	0	0.08256	0.11390
1	0.18994	0.10377	1	0.52350	0.14339
2	0.18791	0.14070	2	0.14436	0.33668
3	0.15173	0.14765	3	0.21204	0.13933
4	0.11097	0.13374	4	0.02239	0.17777
5	0.07732	0.11059	5	0.01425	0.04524
6	0.05270	0.08624	6	0.00069	0.03737
7	0.03564	0.06470	7	0.00020	0.00633
8	0.02411	0.04736	8		0.00353
9	0.01638	0.03413	9		0.00041
10	0.01121	0.02440	10		0.00016
11	0.00730	0.01739	11		0.00001
12	0.00536	0.01241			
13	0.00374	0.00889			
14	0.00258	0.00641			
15	0.00175	0.00465			
16	0.00109	0.00340			
17	0.00056	0.00250			
18	0.00012	0.00185			
19		0.00138			
20		0.00102			
21		0.00075			
22		0.00054			
23		0.00037			
24		0.00023			
25		0.00011			
26		0.00002			

2.4 Neutral beam

The neutral beam was formed through laser photodetachment of a beam of ground-level $C^-(^4S_{3/2})$ that has been mass-to-charge (m/q) selected to be pure $m = 12$. The initial C^- beam was accelerated to a translational energy in the laboratory frame of $E_{C^-} = 26.00$ keV for reaction (1) and 28.00 keV for reaction (2).

The beam was then directed into an electrically isolated floating cell at a voltage of U_f. Inside the floating cell, a few percent of the anion beam underwent photodetachment. After exiting the floating cell, the remaining anion beam was electrostatically removed, leaving a neutral beam of ground-term $C(^3P)$ with a translational energy of $E_C = E_{C^-} + eU_f$, where e is the elementary charge. The fine-structure levels are expected to be statistically populated.[68]

In order to match the H_2^+ beam velocity for reaction (1), we set $U_f = 1.75$ keV, giving the ^{12}C atoms an energy of $E_C = 27.75$ keV (2.31 keV u^{-1}). To match the velocity of D_2^+ for reaction (2), we set $U_f = 0$ keV, giving $E_C = 28.00$ keV (2.33 keV u^{-1}). The U_f values for matched neutral beam and cation beam velocities (v_n and v_i, respectively) were verified by comparing the measured $\langle \sigma v_r \rangle$ *versus* E_r for each reaction for $v_n < v_i$ and $v_n > v_i$ and confirming that the results were symmetric around $E_r = 0$ eV (*i.e.*, $v_n = v_i$). This is discussed in more detail in Section 4.

The neutral beam was collimated using two 5 mm apertures, one located before and the other after the photodetachment

This journal is © the Owner Societies 2020

Phys. Chem. Chem. Phys., 2020, **22**, 27364–27384 | **27367**

region. After the photodetachment region, the beam continued ballistically into the interaction region.

2.5 Interaction region

The interaction region began in the exit of the electrostatic deflector that merged the cations onto the neutrals. Two beam profile monitors (BPMs), one located near the beginning and the other near the end of the interaction region, were used to measure the cross-sectional shape of each beam. Using the BPM measurements, we determined the overlap factor $\langle \Omega(z) \rangle$ of the beams and the bulk angle θ_{bulk} between the two beams. Here z is the nominal axis of copropagation. A Faraday cup in the middle of the interaction region could be used to measure the cation beam current. The beams overlapped for a distance $L = 121.5 \pm 2.5$ cm before they were separated in an electrostatic final analyzer.

The neutral beam density in the interaction region was on the order of 10^3 atoms cm^{-3} and the cation beam density on the order of 10^4 ions cm^{-3}. At such low densities, beam–beam collisions were extremely infrequent, enabling measurements to be carried out in the single-collision regime. In addition, the residual gas pressure was on the order of 10^{-9} Torr ($\sim 3 \times 10^7$ particles cm^{-3}). At these low pressures, parasitic reactions involving either the reactants or products were unimportant.

Reaction (1) formed CH$^+$ product ions with a laboratory translational energy of

$$E_{\text{CH}^+}(U_{\text{f}}) = E_{\text{C}^-} + eU_{\text{f}} + \frac{m_{\text{H}^+}}{m_{\text{H}_2^+}} E_{\text{H}_2^+} = E_{\text{C}^-} + eU_{\text{f}} + 0.5 E_{\text{H}_2^+}. \tag{9}$$

Similarly, reaction (2) formed CD$^+$ ions with a translational energy of

$$E_{\text{CD}^+}(U_{\text{f}}) = E_{\text{C}^-} + eU_{\text{f}} + \frac{m_{\text{D}^+}}{m_{\text{D}_2^+}} E_{\text{D}_2^+} = E_{\text{C}^-} + eU_{\text{f}} + 0.5 E_{\text{D}_2^+}. \tag{10}$$

Here we have ignored the $\sim$eV energy corrections due to any kinetic energy released or internal excitations of the products. These were insignificant compared to the $\sim$keV beam energies.

2.6 Final analyzer

The electrostatic final analyzer consists of a chicane followed by three 90° cylindrical deflectors. The three deflectors included a lower cylindrical deflector (LCD), a middle cylindrical deflector (MCD), and an upper cylindrical deflector (UCD).

The neutral beam traveled ballistically through the chicane (see Fig. 2 of O'Connor et al.[14]), entered the LCD, passed through a hole in the outer electrode of the LCD, and continued into a neutral current detector described below. The transmission efficiency from the interaction region into the neutral detector was $T_{\text{n}} = 0.95 \pm 0.03$.

The end of the interaction region was determined by the first optical element in the chicane, which deflected the reactant cation beam into a Faraday cup. This Faraday cup was used to continuously monitor the cation beam current during data acquisition. Measurements of the cation current before and after the interaction region verified that 100% of the beam was transmitted through the interaction region. The remaining three optical elements of the chicane were used to direct the desired product ions into the LCD.

Product ions were selected for using the translational energy analysis provided for by the three electrostatic cylindrical deflectors, which together had an energy resolution $\Delta E/E = 5\%$, where ΔE is the acceptance energy spread of the analyzer and E the beam energy. The product ion energy varies with U_{f}, as given by eqn (9) and (10), and the applied voltages of the final analyzer were scaled with U_{f} to account for this.

Product ions were detected using a channel electron multiplier (CEM) located at the exit of the UCD. The transmission efficiency through the final analyzer was $T_{\text{a}} = 0.90 \pm 0.05$. A grid with a transmission of $T_{\text{g}} = 0.90 \pm 0.01$ was located at the mouth of the CEM and biased negatively to repel stray electrons. The CEM detection efficiency was $\eta = 0.99 \pm 0.03$.

2.7 Neutral current detector

The neutral atom current, as measured in amperes, was

$$I_{\text{n}} = \frac{I_{\text{NC}}}{\gamma T_{\text{n}}}, \tag{11}$$

where I_{NC} is the negative particle current measured by the neutral cup (NC) and γ is the mean number of negative particles emitted by a neutral particle striking the target inside the NC.

We determined γ using collisional stripping of C$^-$ on He. Measurements were performed for a He gas pressure in the interaction region of 2.8×10^{-4} Torr, using a pressure gauge calibrated for He, and with no He gas, i.e., at a base pressure of $<1.0 \times 10^{-7}$ Torr. The C$^-$ beam current was measured using a Faraday cup, dubbed the upper cup (UC), that is located behind the outer electrode of the MCD. For the appropriate LCD voltages and when the MCD voltages were off, the C$^-$ beam passed through a hole in the outer electrode of the MCD and into the UC. The transmission efficiency into the UC was $T_{\text{UC}} = 0.66 \pm 0.06$. The measured change in the C$^-$ beam current with and without He gas was ΔI_{UC}^-. The corresponding change in the neutral beam current was ΔI_{n} and the measured change in the NC current was ΔI_{NC}. The factor γ could then be written as[69]

$$\gamma = \left(1 + \frac{\sigma_{\text{DED}}}{\sigma_{\text{SED}}}\right) \frac{\Delta I_{\text{NC}}}{\Delta I_{\text{UC}}^-} \frac{T_{\text{u}}}{T_{\text{n}}}. \tag{12}$$

Here, σ_{SED} is the cross section for single electron detachment (SED) of C$^-$ on He forming C and σ_{DED} that for double electron detachment (DED) forming C$^+$.

The DED-to-SED ratio was given by

$$\frac{\sigma_{\text{DED}}}{\sigma_{\text{SED}}} = \frac{\Delta I_{\text{UC}}^+}{\Delta I_{\text{NC}}} \frac{T_{\text{n}}}{T_{\text{u}}}. \tag{13}$$

Here, ΔI_{UC}^+ was the change in the C$^+$ current, measured in the UC using the appropriate polarity voltages on the LCD. This ratio was determined using the same pressures given in the previous paragraph. For each γ measurement, the nearly simultaneous measurement of $\sigma_{\text{DED}}/\sigma_{\text{SED}}$ was used. Averaging over all ten γ measurements, yielded $\sigma_{\text{DED}}/\sigma_{\text{SED}} = 0.077 \pm 0.013$.

27368 | Phys. Chem. Chem. Phys., 2020, **22**, 27364–27384

This journal is © the Owner Societies 2020

It was also important to determine and account for the energy dependence of γ with E_C. For this, we used photodetachment of C^- with E_{C^-} = 28.00 keV and U_f = 0.00 and 4.00 keV, in order to generate a neutral C beam at E_C = 28.00 and 32.00 keV, respectively. No He gas was used in the interaction region for these studies. We found that I_{NC} increased by $\approx 11\%$ going from 28.00 to 32.00 keV, which gave

$$\gamma(E_n \, [\text{keV}]) = 0.05 E_n + 0.60, \qquad (14)$$

for the C + D_2^+ measurement campaign in May 2018 and

$$\gamma(E_n \, [\text{keV}]) = 0.04 E_n + 0.46, \qquad (15)$$

for the C + H_2^+ campaign in January 2019. These fits resulted from averaging multiple measurements on a given day over a series of multiple days. Although both systems were measured at the same values of E_C, γ decreased by $\approx 20\%$ between the two campaigns. We attribute this to changes with time in the surface coating of the target in the neutral cup.

2.8 Laboratory energies and C^+ background suppression

The values of E_{C^-}, U_f, $E_{H_2^+}$, and $E_{D_2^+}$ used were chosen in order to insure that background C^+ formed in the experiment could be readily separated from the signal CH^+ and CD^+ by the final analyzer.

The first source of C^+ arose from C^- that underwent either photodetachment or SED on the residual gas in the floating cell and was subsequently ionized by collisional stripping on the residual gas in the interaction region. The resulting C^+ translational energy was given by

$$E_{C^+}(U_f) = E_{C^-} + eU_f. \qquad (16)$$

This background was easily suppressed using the $\Delta E/E$ = 5% energy resolution of the final analyzer. For reaction (1), the energy separations between the signal and background was

$$\frac{\delta E}{E} = \frac{|E_{CH^+} - E_{C^+}|}{E_{CH^+}} = \frac{0.5 E_{H_2^+}}{E_{CH^+}}. \qquad (17)$$

During data acquisition, U_f was scanned from 0.20 to 4.00 keV. Using eqn (9), the resulting E_{CH^+} ranged from 28.53 to 32.33 keV, giving $\delta E/E \approx 7$–8%. Similarly for reaction (2),

$$\frac{\delta E}{E} = \frac{|E_{CD^+} - E_{C^+}|}{E_{CD^+}} = \frac{0.5 E_{D_2^+}}{E_{CD^+}}. \qquad (18)$$

During data acquisition, U_f was scanned from -1.80 to 2.00 keV. Using eqn (10), the resulting E_{CD^+} spanned from 30.90 to 34.70 keV, giving $\delta E/E \approx 13$–15%. Because $\delta E/E > \Delta E/E$ for each reaction, we were readily able to separate the signal from this background source.

The second source of C^+ arose from C^- that underwent SED on the residual gas before or after the floating cell and was then stripped on the residual gas in the interaction region. (Note that any C^- that underwent DED before or after the floating cell was removed by the beam merger at the entrance to the interaction region and did not contribute to the C^+ background.) The resulting C^+ energy was independent of U_f, giving

$$E_{C^+}(U_f) = E_{C^-}. \qquad (19)$$

This can be a more challenging background to suppress. For example, suppose that we attempted to measure reaction (1) with E_{C^-} = 28.00 keV and U_f = -2.33 keV. From eqn (9) and (19), the resulting $E_{CH^+} = E_{C^+}$ and the signal and background would not be separable.

In order to shift the energy of this second background source so that it differed by more than 5% from the signal-ion energy, we worked with a value of E_{C^-} = 26.00 keV, for reaction (1). This enabled us to still scan U_f symmetrically around $v_n = v_i$. The corresponding E_{C^+} is 8% below the lowest value of E_{CH^+} used here. For reaction (2), the corresponding E_{C^+} is 9% below the lowest value of E_{CD^+} used here.

2.9 Relative energies and beam overlaps

The relative energy, E_r, and beam overlap factors, $\langle \Omega(z) \rangle$, were calculated using the known beam energies, energy spreads, floating cell voltages, beam profiles, and beam trajectories. The bulk angle between the two beams was θ_{bulk} = 0.84 ± 0.33 mrad for reaction (1) and 0.99 ± 0.23 mrad for reaction (2). The minimum values of E_r achieved were E_r = 0.007 ± 0.005 and 0.013 ± 0.009 eV, respectively. At the lowest relative energies, the velocity distribution is nearly Maxwellian. Fits to the velocity distributions for these values of E_r yield temperatures of 55 ± 15 and 101 ± 22 K, respectively. At higher energies the velocity distribution becomes Gaussian with a spread much smaller than v_r.

2.10 Measurement and analysis

Data were collected while scanning U_f over a series of 20 voltage steps. For reaction (1) we scanned U_f over three voltage ranges: 200 to 4000 V in steps of 200 V, 1100 to 3000 V in steps of 100 V, and 1550 to 2500 V in steps of 50 V. For reaction (2) we scanned U_f over four voltage ranges: -1800 to 2000 V in steps of 200 V, -900 to 1000 V in steps of 100 V, -450 to 500 V in steps of 50 V, and -225 to 250 V in steps of 25 V.

At each voltage step, the neutral and cation beams were chopped out of phase in order to extract the desired reaction signal S from the various backgrounds. The uncertainty δS in the extracted signal is given by standard counting statistics, taking into account the signal and various backgrounds involved.

The measured merged-beams rate coefficient from a given scan i and voltage step k is given by

$$\langle \sigma v_r \rangle_{i,k} = \left(\frac{S_{i,k} \pm \delta S_{i,k}}{T_a T_g \eta} \right) \left(\frac{e^2 v_n v_i}{I_n I_i} \right) \left(\frac{1}{L \langle \Omega(z) \rangle} \right). \qquad (20)$$

We measured each of the quantities on the right-hand side of eqn (20), thereby enabling us to present absolute results, independent of any normalization. The various scans were averaged together, as has been detailed in our previous works, to give $\langle \sigma v_r \rangle$ and the corresponding statistical uncertainty $\Delta \langle \sigma v_r \rangle$.

Typical experimental values for the quantities in eqn (20) are given in Table 2, along with their uncertainties. The quantities are grouped into those that vary between voltage steps (Nonconstants) and those that did not vary (Constants). For every E_r,

This journal is © the Owner Societies 2020

Phys. Chem. Chem. Phys., 2020, **22**, 27364–27384 | **27369**

Table 2 Typical experimental values for the quantities of eqn (20) with their corresponding uncertainties

Source	Symbol	Value		Units	Uncertainty (%)
		$C + H_2^+$	$C + D_2^+$		
Non-constants					
Signal rate (statistical)	S	1.6	3.0	s^{-1}	2–25
C velocity	v_n	6.71	6.71	10^7 cm s^{-1}	$\ll 1$
C current	I_n	12	20	nA	5
H_2^+/D_2^+ current	I_i	110	410	nA	5
Overlap factor	$\langle \Omega(z) \rangle$	4.4	2.1	cm^{-2}	10
Neutral detector efficiency	γ	1.6	2.0		6
Constants					
H_2^+/D_2^+ velocity	v_i	6.71		10^7 cm s^{-1}	$\ll 1$
Analyzer transmission	T_a	0.90			5
Grid transmission	T_g	0.90			1
Neutral transmission	T_n	0.95			3
CEM efficiency	η	0.99			3
Interaction length	L	121.5		cm	2
Total systematic uncertainty (excluding the signal rate)					15

Note: the total systematic uncertainty (excluding the statistical error) is calculated treating the individual uncertainties as random sign errors and adding them in quadrature.

the total systematic uncertainty in $\langle \sigma v_r \rangle$ is 15% at an estimated one-sigma accuracy level.

3 Reactant and product channels

3.1 Correlation diagram

Numerous theoretical studies have been conducted on the dynamics of the $C^+(^2P) + H_2(^1\Sigma_g^+) \rightarrow CH^+(^1\Sigma^+) + H(^2S)$ reaction[70–72] and the reverse process[73–76] involving the ground electronic state $1^2A'$ of CH_2^+. However, we are unaware of any such theoretical investigations for the $C(^3P) + H_2^+(^2\Sigma_g)$ reaction, which proceeds through excited states of CH_2^+. These excited electronic states are characterized by a dense manifold of states, due to energetically close states of the $C^+ + H_2/C + H_2^+$ and $CH^+ + H/CH + H^+$ dissociation limits. This makes calculating the potential energy surfaces (PESs) that are needed for QM and QCT dynamics studies particularly challenging for the excited states. In addition, the electronic states may undergo numerous avoided crossings and conical intersections, giving rise to nonadiabatic pathways, which complicate considerably the treatment of the reaction dynamics.

In order to examine the possible reaction pathways relevant to reactions (1) and (2), we report in Fig. 1 the electronic energy diagram for the low lying dissociation limits of the CH_2^+ system corresponding to the $C^+ + H_2$ and $C + H_2^+$ reactant arrangements and the $CH^+ + H$ and $CH + H^+$ product arrangements. The dissociation limits are shown for diatomic molecules in their equilibrium geometry, and exclude the zero-point energy (ZPE) of the reactant and product molecules. The energy ordering of the reactant and product states is based on the experimental term-energy differences and ionization energies of the atoms (Table 3), and the experimental electronic energy terms and dissociation energies of the diatoms (Table 4).

Fig. 1 also shows the CH_2^+ electronic states that correlate adiabatically from the reactant to the product states in C_s
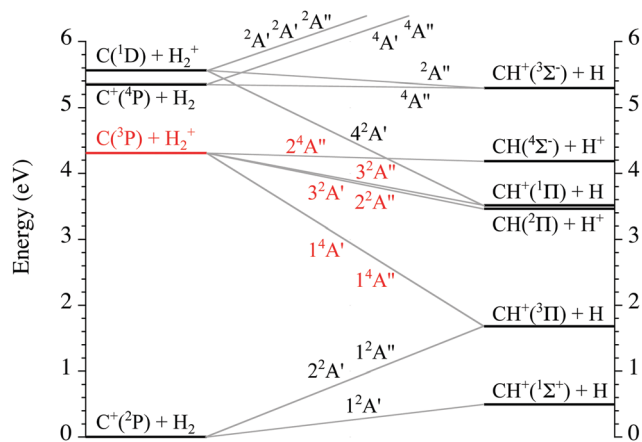

Fig. 1 Electronic energy diagram for the low lying dissociation limits of the CH_2^+ system. The reactant and product arrangements are shown on the left and right sides of the diagram, respectively. The solid lines indicate the correlation of adiabatic electronic states between the reactant and product arrangements in C_s symmetry. The states in red indicate the six electronic states arising from the $C(^3P) + H_2^+(^2\Sigma_g^+)$ reactants considered in the present study. In the figure, H_2 and H_2^+ are in their ground electronic states. Note that while each line connects one reactant state to one product state, these reactant and product states can be connected by several electronic states. These electronic states are degenerate in the reactant and product dissociation limits, but not along the reaction path.

symmetry, which is the point group of interest as the reaction proceeds in the experiment without geometrical restrictions. The correlation is based on the conservation of the total spin and spatial symmetry of the CH_2^+ electronic wave function, and does not take into account the energies of the CH_2^+ reaction intermediates. The equilibrium structures of CH_2^+ are well known for the lowest three doublet states ($1^2A'$, $1^2A''$, and $2^2A'$)[77–79] and the first quartet state ($1^4A''$),[80] but only some of the higher excited states have been characterized.[81,82] Most of the

27370 | *Phys. Chem. Chem. Phys.*, 2020, **22**, 27364–27384

This journal is © the Owner Societies 2020

Table 3 Term-energy differences (ΔE) for C and C$^+$ atoms and ionization energies (IE) of C and H atoms

Term			
Upper	Lower	ΔE^a (eV)	IE^a (eV)
C(^{1}D)	C(^{3}P)	1.260	—
C$^+$(^{4}P)	C$^+$(^{2}P)	5.331	—
C$^+$(^{2}P)	C(^{3}P)	—	11.262
H$^+$	H(^{2}S)	—	13.598

^{a} Experimental values from the National Institute of Standards and Technology[83] (NIST). The term-energy differences and ionization energies of C and C$^+$ were corrected for the fine-structure splittings within each ^{2S+1}L multiplet. The mean energy $\langle E \rangle = \sum_J (2J+1)E_J \big/ \sum_J (2J+1)$ of the $^{2S+1}L_J$ multiplet components was taken to coincide with the energy of the ^{2S+1}L term in the absence of spin–orbit interaction. Here, S and L are the quantum numbers of the total spin and orbital angular momenta, respectively, and J is the total angular momentum quantum number.

equilibrium structures correspond to bent C_{2v} configurations of CH$_2^+$. Relative to the C$^+$(^{2}P) + H$_2$($^1\Sigma_g^+$) limit, the energies reported in the literature lie at −4.32 eV for the $\tilde{X}^2A_1/1^2A'$ ground state,[76]

−4.17 eV for the $\tilde{A}^2B_1(^2\Pi_u)/1^2A''$ state,[78] −1.17 eV for the $\tilde{B}^2B_2/2^2A'$ state,[79] −0.55 eV for the $\tilde{a}^4A_2/1^4A''$ state,[80] +1.7 eV for the $\tilde{C}^2A_2/2^2A''$ state,[82] +2.9 eV for the $\tilde{D}^2A_2/3^2A''$ state,[82] and +3.2 eV for the $2^4A_2(^4\Sigma_u^-)/2^4A''$ state.[81] The states are labeled using both the C_{2v} symmetry (before the slash) and the lower order C_s symmetry (after the slash) to make explicit the connection to the states displayed in Fig. 1. For the case of equilibrium structures corresponding to linear [H–C–H]$^+$ configurations, the $D_{\infty h}$ symmetry is also indicated in the parenthesis. No stable structures have been reported for the $1^4A'$ and $3^2A'$ states. All the above reaction intermediates lie in energy well below the C(^{3}P) + H$_2^+$($^2\Sigma_g^+$) reactants.

The approach of C(^{3}P) to H$_2^+$($^2\Sigma_g^+$) in C_s symmetry gives rise to the six electronic states shown in red in Fig. 1. In the following we investigate which of these states are likely to drive the reaction to the formation of CH$^+$. Since the state of the product ion cannot be probed in the experiment, any state of the CH$^+$ + H product arrangement is a possible outgoing channel for the reaction. Of these six electronic states, the correlation diagram of Fig. 1 shows that the first two quartet

Table 4 Spectroscopic constants for the low lying electronic states of H$_2$, H$_2^+$, CH, and CH$^+$: electronic energy term (T_e), equilibrium dissociation energy (D_e), equilibrium bond length (r_e), vibrational constants (ω_e, $\omega_e x_e$), and rotational constants (B_e, α_e). Experimental values of D_e are deduced from $D_e = D_0 + G(0)$, where D_0 is the dissociation energy and $G(0)$ is the ZPE. Vibrational and rotational constants are given in cm^{-1}. Values in parenthesis are taken from published theoretical works. The MRCI+Q results correspond to the *ab initio* calculations discussed in Section 3.2

|	T_e (eV)	D_e (eV)	r_e (bohr)	ω_e	$\omega_e x_e$	B_e	α_e
H$_2$(X$^1\Sigma_g^+$)							
MRCI + Q	0	4.745	1.401	4402	121	60.8	3.04
Expt.^{a}	0	4.748	1.401	4401	121	60.9	3.06
H$_2^+$(X$^2\Sigma_g^+$)							
MRCI + Q	15.557	2.793	1.997	2323	67	29.9	1.59
Expt.^{a}	15.554^b	2.793	1.988^c	2322	66	30.2	1.68^c
CH(X$^2\Pi$)							
MRCI + Q	0	3.633	2.117	2851	64	14.4	0.54
Expt.^{d}	0	3.64 ± 0.01^a	2.116	2861	64	14.5	0.54
CH(a$^4\Sigma^-$)							
MRCI + Q	0.770	2.862	2.059	3103	72	15.3	0.54
Theory^e	(0.747)	(2.863)	(2.058)	(3091)	(102)	15.4^f	(0.72)
CH$^+$(X$^1\Sigma^+$)							
MRCI + Q	10.607	4.251	2.135	2852	59	14.2	0.50
Expt.^{g}	10.64 ± 0.01^b	4.260^h	2.137	2858	59	14.2	0.50
CH$^+$(a$^3\Pi$)							
MRCI + Q	1.217	3.033	2.146	2678	78	14.0	0.62
Expt.^{i}	(1.204)^j	(3.040)^j	2.147^a	(2684)^j	(79)^j	14.1	0.61
CH$^+$(A$^1\Pi$)							
MRCI + Q	3.006	1.244	2.341	1848	118	11.8	0.92
Expt.^{g}	2.991	1.271^k	2.334^l	1858	109	11.9	0.91
CH$^+$(b$^3\Sigma^-$)							
MRCI + Q	4.814	1.817	2.349	2054	59	11.7	0.57
Expt.^{i}	(4.797)^j	(1.833)^j	2.346	2058	59	11.8	0.56

^{a} Huber and Herzberg.[67] ^{b} T_e value relative to the ground electronic state of the neutral molecule. Experimental T_e values are deduced using the ionization energies of H$_2$ and CH from NIST[83] which have been corrected for the ZPEs of the neutral and cation molecules. ^{c} Theoretical values for $r_e = 1.997$ bohr and $\alpha_e = 1.60$ cm^{-1} from Ishikawa et al.[84] ^{d} Zachwieja.[85] ^{e} Kalemos et al.[86] ^{f} B_e value deduced from $B_e = B_0 + (\alpha_e/2)$, where B_0 is the average rotational constant for the $\nu = 0$ vibrational level, using the experimental value for $B_0 = 15.0$ cm^{-1} from Nelis et al.[87] ^{g} Yu et al.[88] ^{h} Hechtfischer et al.[89] ^{i} Hechtfischer et al.[90] ^{j} Biglari et al.,[91] they obtained $r_e = 2.135$ bohr for CH$^+$(X$^1\Sigma^+$), $r_e = 2.145$ bohr for CH$^+$(a$^3\Pi$), $r_e = 2.341$ bohr for CH$^+$(A$^1\Pi$), and $r_e = 2.351$ bohr for CH$^+$(b$^3\Sigma^-$). ^{k} Helm et al.[92] ^{l} Hakalla et al.[93]

states, $1^4A'$ and $1^4A''$, offer possible adiabatic pathways to CH^+ formation *via* the proton-transfer reaction

$$C(^3P) + H_2^+(^2\Sigma_g^+) \rightarrow CH^+(^3\Pi) + H(^2S), \qquad (21)$$
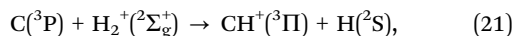
with an associated exoergicity of 2.60 eV.‡ Another possible adiabatic pathway is through the excited doublet state $3^2A''$,

$$C(^3P) + H_2^+(^2\Sigma_g^+) \rightarrow CH^+(^1\Pi) + H(^2S), \qquad (22)$$
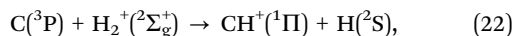
with an exoergicity of 0.81 eV. Note, however, that the $CH^+(^1\Pi)$ + H and $CH(^2\Pi)$ + H^+ limits differ by only ~ 0.03 eV, with similar equilibrium bond lengths for $CH^+(^1\Pi)$ and $CH(^2\Pi)$. Since both products correspond to $(^2A',^2A'')$ states of the same C_s symmetry and spin multiplicity, avoided crossings between the $^2A'$ states and between the $^2A''$ states are expected to develop in the product channel along the C–H internuclear distance, r_{CH}. In such a case, the correlation of the two pairs of $(3^2A',2^2A'')$ and $(4^2A',3^2A'')$ adiabatic states to either the $CH^+(^1\Pi)$ + H or $CH(^2\Pi)$ + H^+ products depends on the length of the C–H bond after dissociation of the CH_2^+ molecule (see Fig. 1 and the lower panel of Fig. 2). Thus, depending on the reaction dynamics, the excited doublet states $3^2A'$ and $2^2A''$ may also contribute to reaction (22). The $4^2A'$ state is involved only through nonadiabatic transitions between $3^2A'$ and $4^2A'$, as it correlates to $C(^1D) + H_2^+(^2\Sigma_g^+)$ reactants and the measurement is performed here with a pure $C(^3P)$ parent beam.

At low collision energies, the reaction is driven at long range by attractive PESs. For collinear approach ($C_{\infty v}$ symmetry), the $C(^3P)$ + $H_2^+(^2\Sigma_g^+)$ reactants give rise to $^{2,4}\Sigma^-$ and $^{2,4}\Pi$ states, corresponding in C_s symmetry to $^{2,4}A''$ and $(^{2,4}A',^{2,4}A'')$ states, respectively. The $^2\Pi$ and $^4\Pi$ states are degenerate at large atom–diatom distances (when spin–orbit interactions are neglected) and correspond to attractive long-range interactions.[40,45] By contrast, long-range interactions are repulsive for the degenerate $^2\Sigma^-$ and $^4\Sigma^-$ states. Accordingly, the attractive $^{2,4}\Pi$ states lie at lower energies than the repulsive $^{2,4}\Sigma^-$ states. Since adiabatic states of same symmetry are ordered according to increasing energy, the PESs for the $3^2A'$ and $2^2A''$ doublet states and the $1^4A'$ and $1^4A''$ quartet states correspond at long range to attractive interaction potentials, whereas the PESs for the $3^2A''$ and $2^4A''$ states correspond to repulsive interactions. This situation should persist whatever the orientation of the reactants or the internuclear distance of H_2^+ because the two main contributions to long-range interactions, namely the charge-quadrupole and charge-induced dipole interactions, involve treating the H_2^+ molecule only as a point charge.

Even though PESs may be attractive at long range, energy barriers at short range can impede the reaction. Information

Fig. 2 Potential energy curves for the low lying electronic states of C + H_2^+ and C^+ + H_2 (upper panel) and CH^+ + H and CH + H^+ (lower panel) as a function of the diatomic bond length. In each case the atom is located at an infinite distance from the diatom. Energies are given relative to the $C^+(^2P)$ + $H_2(^1\Sigma_g^+, r_e)$ dissociation limit. The states potentially relevant to reactions (1) and (2) are displayed in red. H_2 and H_2^+ stand for diatomic molecules in their ground electronic state unless otherwise indicated.

about the short-range behavior of the PESs is thus needed to identify the possible reaction pathways. For the three quartet states, $1^4A'$, $1^4A''$, and $2^4A''$, this information is lacking. For the three doublet states, $3^2A'$, $2^2A''$, and $3^2A''$, the extensive *ab initio* study performed by Sakai *et al.*[82] on the low lying doublet states of CH_2^+ provides valuable information. The $3^2A'$ and $2^2A''$ PESs were found to be barrierless for collinear approach of the reactants (where they form the $2^2\Pi$ PES in $C_{\infty v}$ symmetry). For perpendicular approach, the three doublet PESs exhibit energy barriers above the reactants of up to ~ 0.7 eV for the $3^2A'$ state, ~ 0.2 eV for the $2^2A''$ state, and ~ 1 eV for the $3^2A''$ state. In addition, the energy barrier of the $3^2A'$ PES is present for a wide range of angles of approach of the reactants. The $2^2A''$ and $3^2A''$ PESs were not reported for other orientations of the reactants. Several avoided crossings between the doublet states were also reported by Sakai *et al.*,[82] such as those between $3^2A'$ and $2^2A''$ and the lower $2^2A'$ and $1^2A''$ states, these latter two of which correlate the $C^+(^2P)$ + $H_2(^1\Sigma_g^+)$ reactants with the $CH^+(^3\Pi)$ + H products (see Fig. 1).

---

‡ Here, all exoergicities and endoergicities are reported without ZPE corrections. There are several reasons for this choice. First, sufficient insight is gained from discussing only the ZPE-uncorrected values. It is not necessary to report two different sets of values, one for the reactions with H_2^+ and the other for D_2^+, each of which will have different ZPEs. Second, the ZPEs refer to the $v = 0$ levels but we are dealing with a range of vibrational levels of the parent cations. Lastly, we do not know which of the vibrational levels are most relevant for the reactions being studied, although we do make some hypothesis in Sections 5.3 and 5.4.
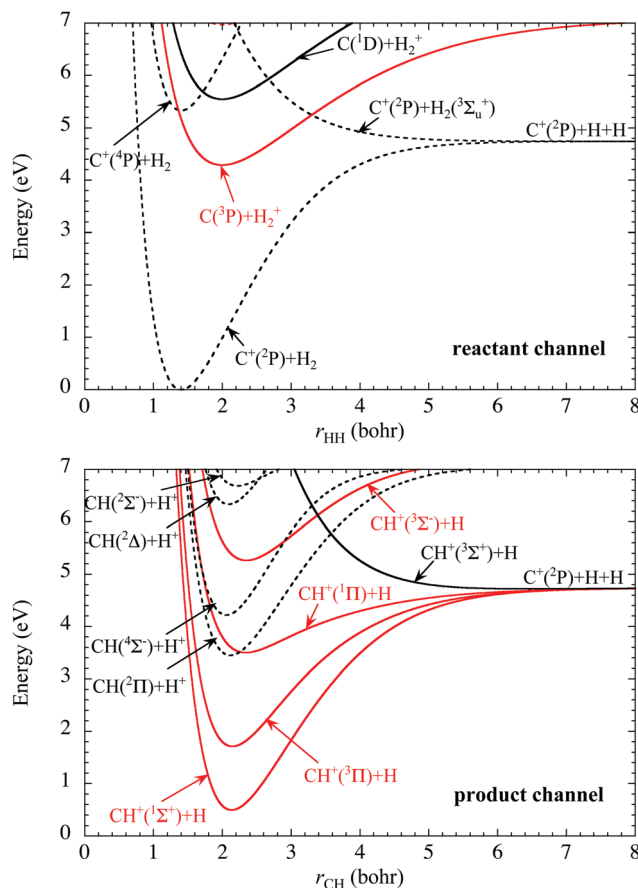
27372 | *Phys. Chem. Chem. Phys.*, 2020, **22**, 27364–27384
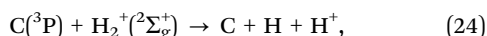
This journal is © the Owner Societies 2020

The repulsive behavior of the $3^2A''$ PES at long range and the relatively large energy barriers of the $3^2A'$, $2^2A''$, and $3^2A''$ PESs at short range in the reactant channel suggest that there is only a minor contribution of doublet states to reactivity at low collision energy. Moreover, multiple nonadiabatic transitions between the doublet PESs may take place along the paths of reaction (22), potentially causing a large part of the reactive flux to bifurcate into the $C^+ + H_2$, $C + H_2^+$ or $CH + H^+$ outgoing channels. Given that the number of close-lying CH_2^+ quartet states is much smaller than for the doublet states, the probability that the quartet states undergo avoided crossings is reduced. It is thus more likely that CH^+ formation proceeds adiabatically through the $1^4A'$ and $1^4A''$ quartet states *via* reaction (21). The attractive behavior of both states at long range, the large reaction exoergicity, and the strong binding energy of $CH_2^+(1^4A'')$ relative to $C(^3P) + H_2^+(^2\Sigma_g^+)$ reactants, are additional features consistent with possible low-energy adiabatic pathways. However, more detailed information on the $1^4A'$ and $1^4A''$ PESs will be needed to provide evidence for the existence of barrierless reaction paths.
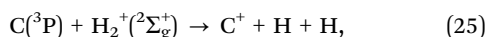
3.2 Asymptotic diatomic potentials

Starting from $C(^3P) + H_2^+(^2\Sigma_g^+)$ reactants, there are several reactive processes which potentially compete with the proton-transfer reaction under study. The possible reaction channels are hydrogen transfer,
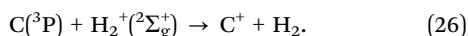
$$C(^3P) + H_2^+(^2\Sigma_g^+) \rightarrow CH + H^+, \qquad (23)$$

collision-induced dissociation (CID),

$$C(^3P) + H_2^+(^2\Sigma_g^+) \rightarrow C + H + H^+, \qquad (24)$$

dissociative CT (DCT),

$$C(^3P) + H_2^+(^2\Sigma_g^+) \rightarrow C^+ + H + H, \qquad (25)$$

and CT,

$$C(^3P) + H_2^+(^2\Sigma_g^+) \rightarrow C^+ + H_2. \qquad (26)$$

Hydrogen transfer can follow adiabatic pathways involving the $3^2A'$ and $2^2A''$ doublet states and the $2^4A''$ quartet state of CH_2^+, leading to form $CH(^2\Pi)$ and $CH(^4\Sigma^-)$ with an exoergicity of 0.84 and 0.07 eV, respectively (see Fig. 1). CID can proceed through two distinct mechanisms:[94] (i) collisional excitation of $H_2^+(^2\Sigma_g^+)$ by $C(^3P)$, leading the highly vibrationally excited H_2^+ to dissociate to $H + H^+$, or (ii) formation of unstable $CH(^2\Pi)$ or $CH(^4\Sigma^-)$ molecules that dissociate to $C + H$. Both of these mechanisms, dissociation of H_2^+ or CH, lead to a CID process that is endoergic by 2.79 eV. DCT can follow the formation of unstable CH^+ molecules that dissociate to $C^+ + H$, similar to CID. But, for DCT, the dissociation of $CH^+(^3\Pi)$ and $CH^+(^1\Pi)$ formed by reactions (21) or (22) gives rise to a process that is endoergic by only 0.46 eV (as is discussed in more detail below). Another possible mechanism[95,96] for DCT involves avoided crossings between CH_2^+ states that correlate to $H_2^+(^2\Sigma_g^+)$ and to a dissociative state of H_2. CT can occur if avoided crossings take place between CH_2^+ states that correlate to $H_2^+(^2\Sigma_g^+)$ and a bound state of the H_2 diatom.[97]

The relative importance of the reaction channels (23)–(26) cannot be determined *a priori*, but knowledge of the asymptotic diatomic potentials of the reactant and product states can be used to predict which processes are likely to occur under experimental conditions. Here, we focus on the DCT and CT processes that may be induced by the vibrational motion of the $H_2^+(^2\Sigma_g^+)$ diatom through avoided crossings. The H_2^+ reactants were formed in an EII source that populated a range of vibrational levels (see Table 1). Previous studies of three-atom ionic systems have shown that vibrational excitation can promote DCT[98–100] and CT[101–103] processes that compete very efficiently with chemical reactions.

For triatomic systems, the PESs can be parameterized as a function of three coordinates describing the relative positions of the nuclei. The reactant and product channels are well suited for using coordinates corresponding to the distance R of the atom to the center of mass of the diatom, the bond length r of the diatom, and the angle between the vectors R and r. When the atom is infinitely far from the diatom, the potential energy varies only as a function of the bond length r. The range of relevant r values depends on the amplitude of the vibrational motion of the diatom. For $R \rightarrow \infty$, cuts through the PESs along the bond coordinate r define potential energy curves (PECs) that correspond to specific electronic states of the atom and diatom fragments, and to degenerate electronic states of CH_2^+ (when spin–orbit interactions are neglected). The PECs associated with different states of the atom and diatom fragments eventually cross at some r values (see Fig. 2). At intermediate values of R, as the reactants approach each other or the products recede from one another, the degeneracy of the CH_2^+ states is lifted under the influence of the atom–diatom interactions. Depending on the symmetry properties of the CH_2^+ states, a crossing along r can turn into an avoided crossing due to mixing of the electronic states. As a result, the adiabatic CH_2^+ states arising from specific fragment states interchange their electronic character as r varies. If the vibrational motion of the diatom allows the nuclei to reach these avoided crossing regions, then new reaction channels (*e.g.*, DCT or CT) are opened up.[95,97]

In order to analyze the asymptotic diatomic limits of the CH_2^+ system, we have carried out *ab initio* calculations for the low lying electronic states of the H_2, H_2^+, CH, and CH^+ diatoms, while varying the diatom internuclear distance from 0.6 to 30 bohr. The PECs associated with the $C + H_2^+$ and $C^+ + H_2$ reactant arrangements and the $CH^+ + H$ and $CH + H^+$ product arrangements were built up from the diatomic potentials using the term-energy differences and ionization energies of the atoms (Table 3). The zero of energy was chosen at the $C^+(^2P) + H_2(^1\Sigma_g^+, r_e)$ dissociation limit, where r_e is the equilibrium bond length of H_2. The *ab initio* energies were computed at the internally contracted multireference configuration interaction[104,105] (MRCI) level, including the Davidson correction[106] (+Q), with state-averaged complete active space self-consistent field[107,108] (CASSCF) reference wave functions. The CASSCF wave functions were built up from the full valence active space of each diatomic species, and the aug-cc-pV6Z (AV6Z) basis

This journal is © the Owner Societies 2020

Phys. Chem. Chem. Phys., 2020, **22**, 27364–27384 | **27373**

set[109,110] was employed. All electronic structure calculations were performed using the MOLPRO suite of programs.[111]

The spectroscopic constants obtained for the electronic states of H_2, H_2^+, CH, and CH^+ are reported in Table 4. The rovibrational constants were determined by fitting, to Dunham-type expansions, a selected set of rovibrational energy levels computed by means of the Fourier Grid Hamiltonian method.[112] Only the main expansion coefficients are reported in Table 4. The agreement of the spectroscopic constants with literature data is thought to be sufficiently accurate to form a realistic picture of the asymptotic diatomic potentials for both the reactant and product states.

The PECs for the low lying electronic states of the $C + H_2^+$ and $C^+ + H_2$ reactants are displayed in the upper panel of Fig. 2 as a function of the H–H diatomic bond length r_{HH}. In the lower panel are shown the PECs for the electronic states of the $CH^+ + H$ and $CH + H^+$ products as a function of the C–H diatomic bond length r_{CH}. Each combination of atomic and diatomic states gives rise to CH_2^+ electronic states which are degenerate for $R \to \infty$ (see Fig. 1). Thus each of the PECs of Fig. 2 corresponds to several degenerate electronic states of CH_2^+.

The upper panel of Fig. 2 shows that the PEC associated with the $C(^3P) + H_2^+(^2\Sigma_g^+)$ reactants undergo two crossings with the PECs of other fragments states. One crossing occurs with the PEC of $C^+(^4P) + H_2(^1\Sigma_g^+)$ at $r_{HH} = 1.36$ bohr, close to the equilibrium geometry of $H_2(^1\Sigma_g^+)$ and midway between the inner classical turning points of the $v = 3$ and $v = 4$ vibrational levels of $H_2^+(^2\Sigma_g^+)$. In C_s symmetry, the $C^+(^4P) + H_2(^1\Sigma_g^+)$ fragments generate one $^4A'$ state and two $^4A''$ states of CH_2^+. Avoided crossings are expected to develop along the bond coordinate r_{HH} between these states and the $1^4A'$, $1^4A''$, and $2^4A''$ quartet states that arise from $C(^3P) + H_2^+(^2\Sigma_g^+)$ as the reactants approach, $i.e.$, as R decreases. Accordingly, the CT reaction

$$C(^3P) + H_2^+(^2\Sigma_g^+) \to C^+(^4P) + H_2(^1\Sigma_g^+) \qquad (27)$$
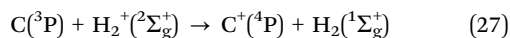
may arise as a consequence of avoided crossings between the quartet states. The CT reaction (27) is endoergic by 1.04 eV. Note that CT can eventually lead to form CH^+ molecules if it is followed by the reaction

$$C^+(^4P) + H_2(^1\Sigma_g^+) \to CH^+(^3\Sigma^-) + H(^2S). \qquad (28)$$
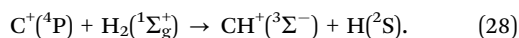
The process is slightly exoergic (~ 0.08 eV) and can proceed adiabatically through an excited $^4A''$ quartet state of CH_2^+ (see Fig. 1). Furthermore there is experimental evidence[113] for the production of $CH^+(^3\Sigma^-)$ from $C^+(^4P) + H_2(^1\Sigma_g^+)$ reactants.

A second crossing occurs with the PEC of $C^+(^2P) + H_2(^3\Sigma_u^+)$ at $r_{HH} = 3.30$ bohr, close to the outer classical turning point of the vibrational level $v = 3$ of $H_2^+(^2\Sigma_g^+)$. The $C^+(^2P) + H_2(^3\Sigma_u^+)$ fragments give rise to two $^2A'$ states, one $^2A''$ state, two $^4A'$ states, and one $^4A''$ state, all in C_s symmetry. Thus avoided crossings can occur with the $3^2A'$ and $2^2A''$ doublet states and the $1^4A'$ and $1^4A''$ quartet states of $C(^3P) + H_2^+(^2\Sigma_g^+)$. Since the PEC of $C^+(^2P) + H_2(^3\Sigma_u^+)$ is purely repulsive, these avoided crossings may lead to the DCT process

$$C(^3P) + H_2^+(^2\Sigma_g^+) \to C^+(^2P) + H(^2S) + H(^2S). \qquad (29)$$
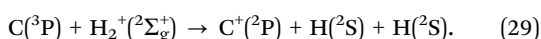
When this DCT mechanism occurs in the reactant channel via predissociation of the bound states of $H_2^+(^2\Sigma_g^+)$ through the $H_2(^3\Sigma_u^+)$ dissociative state, it is referred to in the literature as collision-induced predissociation (CIP).[98–100] The DCT process (29) is endoergic by 0.46 eV, but the crossing at $r_{HH} = 3.30$ bohr forms an energy barrier to CIP along the vibrational degree of freedom of $H_2^+(^2\Sigma_g^+)$ that lies at +0.96 eV above the reactants.

The CT reaction (27) and DCT reaction (29) have yet to be studied, and their impact on the reaction of CH^+ formation cannot be predicted solely from the asymptotic diatomic potentials. From previous studies[101–103,114] of similar $A + BC^+ \rightleftharpoons A^+ + BC$ processes, we can only anticipate a propensity for the CT reaction (27) to be more efficient for the case of near resonance between the $C(^3P) + H_2^+(^2\Sigma_g^+,v)$ and $C^+(^4P) + H_2(^1\Sigma_g^+,v')$ energy levels. Likewise, the results of previous works on CIP[98–100,115,116] suggest that the DCT reaction (29) might be more efficient for the $H_2^+(^2\Sigma_g^+,v)$ vibrational states lying close in energy to the curve crossing. These points will be discussed further in Section 5.

Moving now to the product channels, the PECs for the low lying electronic states of $CH^+ + H$ and $CH + H^+$ are displayed in the lower panel of Fig. 2. As can be seen, the PEC of the $CH^+(^3\Pi) + H$ products does not undergo any crossing with the PECs of other product states. This indicates that all the reactive flux driven by the $1^4A'$ and $1^4A''$ adiabatic PESs can lead to the formation of $CH^+(^3\Pi)$. Therefore, reaction channel (21) could be highly relevant to CH^+ formation for those $H_2^+(^2\Sigma_g^+,v)$ reactants that are weakly influenced by the CT reaction (27) and DCT reaction (29). Another important feature shown in Fig. 2 is the curve crossing at $r_{CH} = 2.26$ bohr between the PECs of $CH^+(^1\Pi) + H$ and $CH(^2\Pi) + H^+$. Since each product corresponds to a pair of $(^2A',^2A'')$ doublet states, avoided crossings between the two pairs of states are expected to occur as the product fragments recede from one another. As a result, the ratio between the $CH^+(^1\Pi)$ and $CH(^2\Pi)$ products molecules following the proton-transfer reaction (22) and the hydrogen-transfer reaction

$$C(^3P) + H_2^+(^2\Sigma_g^+) \to CH(^2\Pi) + H^+, \qquad (30)$$
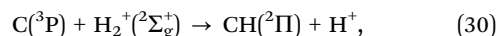
should largely depend on nonadiabatic transitions between the doublet states. Finally, it is worth noting that the PECs of both the $CH^+(^3\Pi) + H$ and $CH^+(^1\Pi) + H$ products correlate to $C^+(^2P) + H(^2S) + H(^2S)$ fragments at large r_{CH} distance. Consequently, both reaction pathways (21) and (22) can give rise to the DCT reaction (29) when the CH^+ molecules are formed with an internal energy greater than the dissociation energy of the $CH^+(^3\Pi)$ and $CH^+(^1\Pi)$ products. The DCT channel (29) is endoergic by only 0.46 eV, as mentioned earlier. Moreover, unlike the reactant channel, there are no avoided crossings in the product channel to produce a potential energy barrier along the dissociation pathway (see Fig. 2). As a result of the low energy threshold for DCT in the product channel, this process might have a significant impact on the reaction under study.

4 Results

Our measured merged-beams rate coefficient $\langle \sigma v_r \rangle$ for reactions (1) and (2) are shown in Fig. 3 as a function of the collision energy E_r. The data are also given in Tables 5 and 6, respectively. The excellent agreement of our results for $v_n < v_i$ and $v_n > v_i$, for each reaction, verifies the accuracy of our E_r scale.

In Fig. 4, we show the same results for the merged-beams energy-weighted cross section $\langle \sigma E_r^{1/2} \rangle$. This removes both the v_r^{-1} dependence of the cross section and that of the differing reduced masses for reactions (1) and (2), thereby enabling us to best explore the subtleties in the reactive scattering process.

Lastly, Fig. 5 presents the merged-beams cross section for reactions (1) and (2). The cross section was extracted from our measurements using $\sigma = \langle \sigma v_r \rangle / \langle v_r \rangle$, where $\langle v_r \rangle$ is the merged-beams average value of v_r at E_r.

5 Discussion

5.1 Comparison to earlier measurements

Reaction (2) was measured by Schuette and Gentry[40] during their pioneering series of merged-beams studies of neutral atoms reacting with molecular cations. We find that our results for the energy dependence of the merged-beams rate coefficient are in excellent agreement with those of Schuette and Gentry for $E_r > 0.03$ eV. At lower values of E_r, the data extracted from merged beams experiments are very sensitive to the bulk angle between the two beams that is used in the analysis (see Section 2.9). The differences that are seen here below 0.03 eV may potentially be explained by an underestimation of the bulk angle in the experiment of Schuette and Gentry.
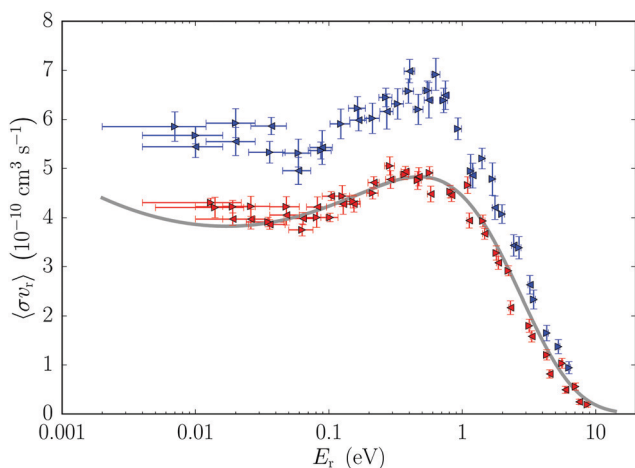
Fig. 3 Merged-beams rate coefficients $\langle \sigma v_r \rangle$ as a function of the relative translational energy E_r. The present results for the C + H_2^+ → CH^+ + H reaction (1) are shown in blue and those for the C + D_2^+ → CD^+ + D reaction (2) are shown in red. The leftward pointing triangles correspond to $v_n < v_i$ and the rightward pointing triangles to $v_n > v_i$. The vertical error bars represent the statistical uncertainty and the horizontal error bars show the energy spread at each E_r. The gray solid line corresponds to 0.796 times the experimental results of Schuette and Gentry[40] for reaction (2).

Table 5 Experimental results for C + H_2^+ → CH^+ + H: listing of the experimental merged-beams rate coefficients, $\langle \sigma v_r \rangle$, with corresponding one-sigma statistical uncertainties, $\Delta \langle \sigma v_r \rangle$, as a function of the relative translational energy, E_r, with the one-sigma width of the collision-energy spread, ΔE_r, vs. applied floating cell voltages, U_f

U_f (kV)	E_r (eV)	ΔE_r	$\langle \sigma v_r \rangle$ (10^{-10} cm³ s⁻¹)	$\Delta \langle \sigma v_r \rangle$
0.200	3.211	0.105	2.630	0.189
0.400	2.429	0.092	3.434	0.220
0.600	1.758	0.078	4.204	0.240
0.800	1.198	0.064	4.858	0.249
1.000	0.747	0.051	6.494	0.293
1.100	0.562	0.044	6.394	0.363
1.200	0.403	0.037	6.984	0.235
1.300	0.272	0.031	6.162	0.358
1.400	0.167	0.024	5.986	0.219
1.500	0.089	0.017	5.428	0.346
1.550	0.059	0.014	4.952	0.274
1.600	0.037	0.011	5.865	0.176
1.650	0.020	0.008	5.548	0.286
1.700	0.010	0.006	5.442	0.220
1.750	0.007	0.005	5.854	0.300
1.800	0.010	0.006	5.674	0.173
1.850	0.020	0.008	5.925	0.295
1.900	0.036	0.011	5.329	0.221
1.950	0.059	0.014	5.313	0.284
2.000	0.087	0.017	5.365	0.173
2.050	0.123	0.021	5.909	0.304
2.100	0.164	0.024	6.229	0.237
2.150	0.212	0.027	6.023	0.310
2.200	0.267	0.030	6.449	0.189
2.250	0.328	0.034	6.318	0.312
2.300	0.395	0.037	6.578	0.248
2.350	0.468	0.040	6.205	0.308
2.400	0.547	0.043	6.591	0.194
2.450	0.633	0.047	6.918	0.324
2.500	0.725	0.050	6.388	0.249
2.600	0.928	0.056	5.809	0.223
2.700	1.155	0.063	4.947	0.338
2.800	1.408	0.069	5.203	0.211
2.900	1.684	0.076	4.784	0.329
3.000	1.985	0.083	4.074	0.191
3.200	2.660	0.095	3.387	0.227
3.400	3.431	0.108	2.333	0.189
3.600	4.297	0.121	1.652	0.158
3.800	5.256	0.134	1.374	0.143
4.000	6.309	0.147	0.943	0.124

On an absolute scale, our results are smaller than those of Schuette and Gentry[40] by a factor of 0.796 ± 0.004. This scaling factor was determined by a least-squares fit of the ratio of our merged-beams rate coefficients to theirs for $E_r > 0.03$ eV. The smallness of the fit uncertainty highlights the excellent agreement that we see in the energy dependence for reaction (2). In Fig. 3–5, we show their scaled results. As discussed in Section 1, their neutral C beam contained an unknown fraction of metastable C atoms, due to the CT method used to produce the neutral beam. The photodetachment method that we have used here produced a beam of essentially 100% pure ground-term C(^{3}P). Schuette and Gentry reported their final results for what they took to be a beam of pure ground-term C(^{3}P), but they could not rule out metastable contamination. They also presented systematic studies into the effects of metastable atoms, finding that the cross section for reactions with

This journal is © the Owner Societies 2020

Phys. Chem. Chem. Phys., 2020, 22, 27364–27384 | 27375

Table 6 Same as Table 5 but for C + D$_2^+$ → CD$^+$ + D

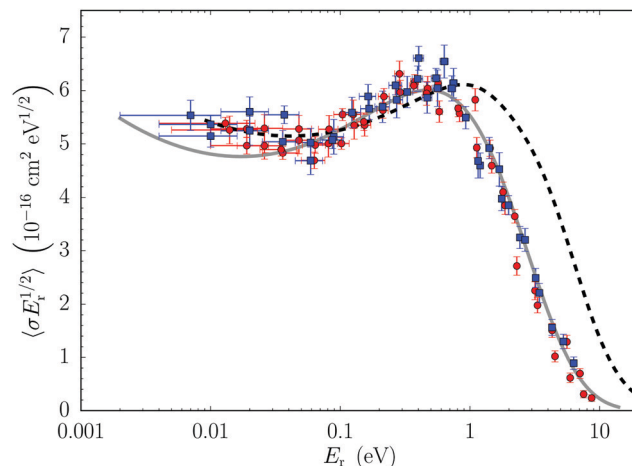| U_f (kV)	E_r (eV)	ΔE_r	$\langle \sigma v_r \rangle$ (10^{-10} cm^3 s^{-1})	$\Delta \langle \sigma v_r \rangle$
−1.800	7.529	0.116	0.246	0.053
−1.600	5.930	0.103	0.492	0.071
−1.400	4.527	0.090	0.816	0.083
−1.200	3.317	0.077	1.583	0.114
−1.000	2.299	0.064	2.169	0.139
−0.900	1.862	0.058	3.079	0.134
−0.800	1.471	0.052	3.672	0.112
−0.700	1.128	0.045	3.942	0.153
−0.600	0.831	0.039	4.457	0.126
−0.500	0.580	0.033	4.484	0.161
−0.450	0.472	0.030	4.832	0.183
−0.400	0.375	0.027	4.936	0.105
−0.350	0.290	0.024	4.775	0.178
−0.300	0.217	0.021	4.711	0.120
−0.250	0.154	0.018	4.280	0.165
−0.225	0.128	0.017	4.278	0.207
−0.200	0.104	0.015	4.440	0.090
−0.175	0.082	0.014	4.219	0.207
−0.150	0.064	0.013	3.982	0.124
−0.125	0.048	0.012	4.054	0.204
−0.100	0.036	0.011	3.862	0.096
−0.075	0.026	0.010	3.971	0.202
−0.050	0.019	0.009	3.973	0.126
0.000	0.013	0.009	4.308	0.089
0.025	0.014	0.009	4.208	0.208
0.050	0.019	0.009	4.224	0.129
0.075	0.026	0.010	4.233	0.205
0.100	0.035	0.011	3.913	0.095
0.125	0.048	0.012	4.223	0.206
0.150	0.063	0.013	3.751	0.123
0.175	0.081	0.014	4.004	0.202
0.200	0.102	0.015	4.005	0.086
0.225	0.126	0.017	4.442	0.215
0.250	0.152	0.018	4.331	0.132
0.300	0.213	0.021	4.503	0.119
0.350	0.286	0.024	5.052	0.186
0.400	0.369	0.027	4.875	0.105
0.450	0.463	0.029	4.758	0.179
0.500	0.568	0.032	4.909	0.126
0.600	0.811	0.038	4.534	0.128
0.700	1.098	0.044	4.662	0.168
0.800	1.428	0.051	3.934	0.121
0.900	1.800	0.057	3.280	0.145
1.000	2.216	0.063	2.916	0.102
1.200	3.175	0.075	1.799	0.133
1.400	4.302	0.087	1.205	0.105
1.600	5.596	0.099	1.034	0.100
1.800	7.055	0.111	0.557	0.073
2.000	8.678	0.123	0.189	0.048

Fig. 4 Merged-beams energy-weighted cross section $\langle \sigma E_r^{1/2} \rangle$ as a function of the relative translational energy E_r. The present results for reaction (1) are shown by the blue squares and for reaction (2) by the red circles. The gray solid line corresponds to 0.796 times the experimental results of Schuette and Gentry[40] for reaction (2). The dashed black curve shows our earlier experimental results[14] for C + H$_3^+$ forming either CH$^+$ via reaction (31) or CH$_2^+$ via reaction (32), multiplied by a factor of 0.463.
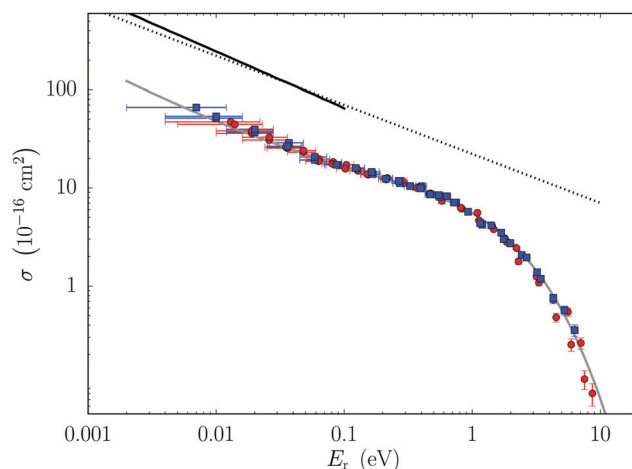

Fig. 5 Merged-beams cross sections as a function of the relative translational energy E_r. The present results for reaction (1) are shown by the blue squares and for reaction (2) by the red circles. The gray solid line corresponds to 0.796 times the experimental results of Schuette and Gentry[40] for reaction (2). The black dotted line shows the theoretical LGS capture cross section σ_α corresponding to a pure charge-induced dipole interaction potential. The black solid line shows the average capture cross section $\sigma_{\Theta\alpha}$ calculated by Schuette and Gentry[40] from interaction potentials that include charge-quadrupole and charge-induced dipole contributions and incorporate the effects of spin–orbit interactions.[45] See Section 5.4 for details.

metastable atoms was smaller than that for ground-term atoms. The experimentally determined cross section is inversely proportional to the atom current (see, e.g., eqn (20)). Hence, if their atom beam were partly contaminated by less-reactive metastables, then the effective atom particle current would be correspondingly reduced and the measured signal would lead to a larger experimental cross section. Their results, therefore, represent a lower limit for a pure beam of C(^{3}P). That we measured a cross section that agrees to within ≈20% indicates that Schuette and Gentry did indeed have a beam of nearly pure C(^{3}P). We attribute the ≈20% difference between their results and ours as likely being due to the combined experimental uncertainty of ±13% for their merged-beams

method[117] and ±15% for our present work. Hence, the factor of ∼4 difference between their experimental results and their LGS-type capture model is extremely unlikely to be due to unknown experimental errors. We discuss the likely cause for the difference in more detail in Section 5.4.

The absence of an energy threshold and the monotonic decrease of the cross section with increasing E_r, shown in Fig. 5,

are typical features of barrierless exoergic reactions. For such reactions, we expect the reactivity at low E_r to be mainly determined by the long-range interactions, which are here dominated by the charge of H_2^+ interacting with the permanent quadrupole moment and the induced electric dipole moment of the carbon atom.

Since the cation molecule is involved only as a point charge at long range, it is interesting to compare our present experimental results to our earlier measurements[14] for the barrierless exoergic reactions

$$C(^3P) + H_3^+(^1A_1') \rightarrow CH^+ + H_2, \tag{31}$$

and

$$C(^3P) + H_3^+(^1A_1') \rightarrow CH_2^+ + H. \tag{32}$$
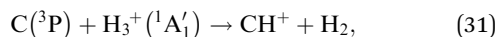
The merged-beams energy-weighted cross section for reaction (1) is compared in Fig. 4 to the scaled sum of the energy-weighted cross sections measured for reactions (31) and (32). A least-squares fit of the ratio of the energy-weighted cross section for reaction (1) to the sum of that for reactions (31) and (32) for $E_r \lesssim 0.06$ eV yields a scaling factor of 0.463 ± 0.007.

Fig. 4 shows that the behavior of $\langle \sigma E_r^{1/2} \rangle$ *versus* E_r for reaction (1) is similar to that measured for the sum of reactions (31) and (32). From the lowest E_r measured up to about 0.06 eV, $\langle \sigma E_r^{1/2} \rangle$ shows the same monotonic decrease with increasing E_r for both H_2^+ and H_3^+. This is expected, as all three barrierless exoergic reactions are driven by the same dominant interactions at long range between the $C(^3P)$ and the charge of the cation. The scaling factor between the H_2^+ and H_3^+ results is likely due to a combination of several factors. Here we mention some of these factors, but a complete quantitative explanation is beyond the scope of this paper. Experimental limitations are one issue that would need to be taken into account, namely that for H_2^+ we have not measured the exoergic hydrogen-transfer reaction (23), leading to CH products. Thus, our measurements do not account for the complete reactivity of $C(^3P) + H_2^+$. This is to be contrasted with the $C(^3P) + H_3^+$ reaction, where the hydrogen-transfer channel is endoergic by 2.69 eV[14] and does not contribute to the reactivity at these low energies. The magnitude of the scaling factor may also be due to potential restrictions in the range of the H_2^+ internal states contributing to reaction (1) as well as in the number of CH_2^+ electronic states that drive the reaction. The influence of these two effects on reaction (1) is discussed in Section 5.4.

Coming back to the behavior of $\langle \sigma E_r^{1/2} \rangle$ *versus* E_r, starting at $E_r \sim 0.06$ eV, the energy-weighted cross sections measured for H_2^+ and H_3^+ begin to increase with increasing E_r. For the H_3^+, though, this increase is only seen in reaction (31) and not reaction (32). The increases seen for reactions (1) and (31) indicate a change in the energy dependence of the reaction cross sections. The reason for this change is unclear at present. But it is quite striking that the two different collision systems display similar trends starting at nearly the same energy. Additional theoretical and experimental work is needed to explore possible candidate explanations for this feature.

Lastly, from $E_r \sim 0.4$ eV, $\langle \sigma E_r^{1/2} \rangle$ for reactions (1) and (2) turns over and decreases over the next decade or so in energy, till it reaches values too small for us to measure. The smooth fall-off is due to the internal excitations of the parent cations, which produce a gradual opening of the endoergic channels that compete with the proton-transfer reaction. For reactions (1) and (2), the onset of the fall-off almost coincides with the threshold of the endoergic DCT channel (29) at 0.46 eV. The internal energy of the parent cations leads to a shift to lower E_r for the opening of this first competing channel. The slight shift observed in Fig. 4 suggests that the main contribution to reactions (1) and (2) is from H_2^+ and D_2^+ molecules with low internal energy. For reactions (31) and (32), the onset of the fall-off is also shifted to lower E_r relative to the opening of the first competing endoergic channel at 1.98 eV. This shift was attributed to the internal excitation of the H_3^+ reactants, as discussed in detail in O'Connor *et al.*[14]

Another interesting finding of our experimental results is the apparent absence of an intermolecular isotope effect for reactions (1) and (2). To within the experimental uncertainties, our cross section results for H_2^+ and D_2^+ are almost identical, as can be seen in Fig. 4 and 5. A similar lack of an intermolecular isotope effect was found for our $C + H_3^+$ results compared to those Savić *et al.*[118] for the $C + D_3^+$ reaction.

5.2 Astrophysical implications

Our experimental findings have potentially useful implications for improving deuterated astrochemical models for interstellar molecular clouds,[119–125] which have typical densities of 10^4–10^6 cm^{-3} and temperatures of $\sim$10–100 K. At these low densities, three-body processes are unimportant and the gas-phase chemistry is driven by bimolecular reactions. The low temperatures mean that there is insufficient translational energy available to overcome the activation barriers typical of many neutral–neutral reactions. Hence much of the gas-phase chemistry is driven by barrierless and exoergic ion-neutral chemistry.

Deuterated molecular species are powerful diagnostics for probing the physical properties of cold molecular clouds because of their high relative abundance at low temperatures. This chemical fractionation results from the ZPE of deuterated molecules being lower than that of the normal isotope, typically by up to several hundred K. Hence, at sufficiently cold temperatures, exoergic D-substitution reactions go forward, but the endoergic H-substitution reverse reactions do not. This fractionation process explains the observed abundance ratios of D-bearing species relative to their H-bearing analogues that are orders of magnitude larger than the interstellar D/H ratio of $\sim$1.6 $\times$ 10^{-5} (set initially by Big Bang Nucleosynthesis, but slowly reduced since then by astration, namely the destruction of D in stars).

A major challenge in constructing deuterated astrochemical models is that the vast majority of the chemical data available are from studies of reactions involving H-bearing species. The astrochemists need guidance on how to convert these existing chemical data for H-bearing species into that for D-bearing species.

We have found that there is an apparent absence of an intermolecular isotope effect for barrierless exoergic reactions involving either H_2^+ or H_3^+ and a neutral atom. Building on this finding, our work suggests that the cross section *versus* E_r data for such reactions with H_2^+ and H_3^+ can be used, without any scaling needed, for fully deuterated species D_2^+ and D_3^+. It remains an open question if this scaling is also valid for other barrierless exoergic ion-neutral reactions invovling not just neutral atoms, but also neutral non-polar molecules. But our finding matches what is expected for barrierless exoergic reactions that do not depend on the initial rovibrational state of the parent cations.[24,27]

5.3 Competing endoergic channels

The H_2^+ and D_2^+ molecules that are formed in the EII ion source are vibrationally and rotationally excited (see Table 1). Not all of the $H_2^+(v,j)$ and $D_2^+(v,j)$ rovibrational states are expected to contribute to reactions (1) and (2), respectively, primarily because of the competition with the CT reaction (27) and DCT reaction (29), and their fully deuterated analogues. The PECs for the electronic states relevant to these latter two processes are shown in Fig. 6, together with the vibrational energy levels associated with the bound states of the cation and neutral molecules.

Here, we focus on vibrational excitation because it plays a major role in inducing the CT and DCT processes. Additionally, in the experiment, the rotational excitation of the cation molecules is relatively low. Approximately 95% of the initial rovibrational population of the cation beam is in $H_2^+(v,j \leq 3)$ for reaction (1) and $D_2^+(v,j \leq 5)$ for reaction (2). The increase of internal energy due to this level of rotational excitation is at most 0.05 eV. The effect of rotational excitation on the translational and vibrational motion of the reactants through the centrifugal barriers is also expected to be weak due to the small rotational quantum numbers involved.

The rovibrational population distribution of H_2^+ and D_2^+ should remain almost unchanged as the reactants approach at low collision energies. Because long-range interactions are primarily isotropic and independent of the diatomic bond length r_{HH}, energy transfer between the translational motion of the reactants and the rovibrational motions of the cation molecules is expected to be weak. Under these circumstances, the asymptotic PECs and vibrational energies shown in Fig. 6 can serve to qualitatively evaluate the relative importance of CT and DCT on the various reactant states.

At low collision energies, the CT channel (27) is energetically allowed for $H_2^+(v \geq 5)$ and $D_2^+(v \geq 7)$, as can be seen in Fig. 6. For most of these reactant states, we expect the CT process to be negligible, due to large mismatch between the $C(^3P) + X_2^+(^2\Sigma_g^+,v)$ and $C^+(^4P) + X_2(^1\Sigma_g^+,v')$ energy levels (X = H, D). CT is likely to be efficient only for $H_2^+(v = 5)$, $D_2^+(v = 9)$, and $D_2^+(v = 12)$ due to near resonance with $C^+(^4P) + X_2(^1\Sigma_g^+,v')$ energy levels. But because these states are not significantly populated in our cation source, CT is not expected a major competing process.

The DCT reaction channel (29) is energetically allowed for $H_2^+(v \geq 2)$ and $D_2^+(v \geq 2)$ even at the lowest collision energies, as shown in Fig. 6. The DCT process can take place during the
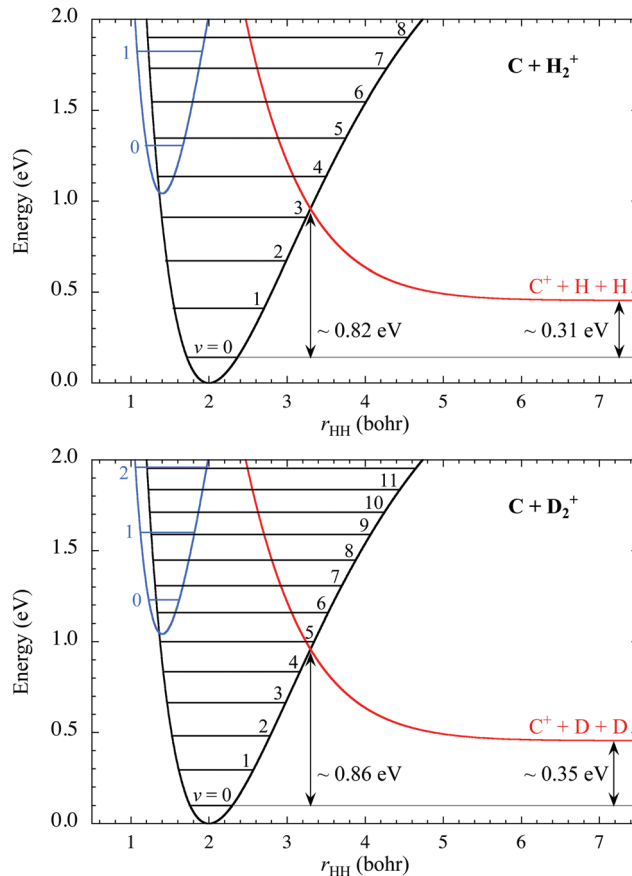

Fig. 6 Potential energy curves for the electronic states of $C(^3P) + H_2^+(^2\Sigma_g^+)$ (black line), $C^+(^4P) + H_2(^1\Sigma_g^+)$ (blue line), and $C^+(^2P) + H_2(^3\Sigma_u^+)$ (red line) as a function of the diatomic bond length r_{HH}. The carbon atom/ion is located at an infinite distance from the diatom. Energies are given relative to the $C(^3P) + H_2^+(^2\Sigma_g^+,r_e)$ dissociation limit. The upper panel shows the vibrational energy levels of $H_2^+(^2\Sigma_g^+,v)$ and $H_2(^1\Sigma_g^+,v')$. The lower panel shows the vibrational energy levels of $D_2^+(^2\Sigma_g^+,v)$ and $D_2(^1\Sigma_g^+,v')$.

approach of the reactants (*i.e.*, in the reactant channel) through the avoided crossing between the electronic states that correlate to $C(^3P) + H_2^+(^2\Sigma_g^+)$ and $C^+(^2P) + H_2(^3\Sigma_u^+)$. This dissociation mechanism is referred to in the literature as CIP.[98–100] Here, the relatively large energy barrier along r_{HH} formed by the avoided crossing should impede dissociation by tunneling for those reactant states lying well below the curve crossing. Additionally, the fast vibrational motion through the avoided crossing region should impede dissociation through nonadiabatic transitions for the reactant states lying well above the curve crossing. Therefore, CIP is expected to be efficient only for those states lying close in energy to the curve crossing. Accordingly, the asymptotic PECs shown in Fig. 6 suggest that the $H_2^+(v = 3, 4)$ and $D_2^+(v = 4, 5, 6)$ states are the most likely to dissociate by CIP. We must note, however, that the location and shape of the avoided crossing region is highly sensitive to the amount of mixing of the electronic states and to the behavior of the PESs as the reactants approach. Thus, the range of reactant states likely to dissociate by CIP cannot be unambiguously identified using solely the asymptotic PECs.

27378 | *Phys. Chem. Chem. Phys.*, 2020, **22**, 27364–27384

This journal is © the Owner Societies 2020

The DCT process (29) can also take place in the product channel when the CH$^+$ molecules are formed with an internal energy greater than their dissociation energy. Above the energy threshold for DCT, the formation of stable CH$^+$ molecules requires that the excess energy relative to the C$^+$(^{2}P) + H(^{2}S) + H(^{2}S) dissociation limit be released as translational energy of the products. For reaction (2), Schuette and Gentry[40] have measured the translational exoergicity

$$Q = (E'_r - E_r), \tag{33}$$

where E_r and E'_r are the translational energy of the reactants and products, respectively. They reported a mean value $\bar{Q}$ which increases slightly from $\bar{Q} \sim 0.3$ eV at $E_r = 0.002$ eV to $\bar{Q} \sim 0.6$ eV at $E_r = 0.1$ eV, and then remains approximately constant up to $E_r = 3$ eV. At 0.002 eV, the distribution of product translation energies is sufficiently narrow[40] that the range of reactant states providing the main contribution to reaction can be inferred from the measured $\bar{Q}$. Using conservation of the total energy, the translational exoergicity can be written as,

$$Q = U_i - U_f + \Delta E, \tag{34}$$

where U_i and U_f are the internal (vibrational and rotational) energies of the reactant and product molecules, respectively, and ΔE is the energy difference between the reactant and product dissociation limits. For a given reaction channel ΔE, we can then determine for each reactant state U_i a lower limit Q_{min} for Q that is consistent with the formation of stable CH$^+$ molecules, taking into account that the internal energy U_f cannot exceed the dissociation energy D_e of the product molecule. Using the potential energy curves of Fig. 2 and 6 to calculate the energetic quantities involved in eqn (34), we find that $Q_{min} \leq \bar{Q} \sim 0.3$ eV only for the D$_2^+$($v \leq 3$) states, *i.e.*, only these states can lead to form stable CD$^+$ molecules given the measured translational exoergicity at $E_r = 0.002$ eV. Assuming a similar value of $\bar{Q}$ for reaction (1), we find that only the H$_2^+$($v \leq 2$) states are able to form stable CH$^+$ molecules at low E_r. The moderate increase of $\bar{Q}$ from 0.3 to 0.6 eV as E_r increases from 0.002 to 0.1 eV, and the nearly constant value of $\bar{Q}$ from 0.1 to 3 eV, indicate that only a few additional reactant states can contribute to reactions (1) and (2) at higher collision energies.

The translational exoergicity measured by Schuette and Gentry[40] does not allow one to discriminate the individual contributions of reaction channels (21) and (22), since the electronic states involved in both reactions share the same C$^+$(^{2}P) + H(^{2}S) + H(^{2}S) dissociation limit. However there are several features of the CH$_2^+$ electronic system (see Section 3.1) which suggest that there is only a minor contribution from reaction (22) at low E_r. If reaction (21) is indeed the dominant channel, then the large reaction exoergicity of 2.60 eV and the small value of $\bar{Q}$ indicate that the CH$^+$($^3\Pi$) molecules would be preferentially formed close to their dissociation limit. If that is the case, then the negligible contribution of H$_2^+$($v \geq 3$) and D$_2^+$($v \geq 4$), inferred from both the asymptotic PECs and the measured translational exoergicity, may be due not only to CIP

during the reactant approach, but also to DCT resulting from an increased amount of energy being released into the vibrational mode of CH$^+$($^3\Pi$).

We also note that rovibrationally excited CH$^+$($^3\Pi$) molecules can be formed with internal energies lying above the dissociation limit. Such molecules are temporarily bound by the centrifugal barrier that results from the rotational motion of the product molecules. The finite lifetime of these quasibound molecules is determined by their tunneling rate through the centrifugal barrier. The flight time from the interaction region to the detector was on the $\sim\mu$s order for the measurements of Schuette and Gentry[40] and for our work here. Quasibound molecules with lifetimes longer than this can contribute to the measured reaction signal before they undergo DCT, thereby leading to an artificial enhancement of the reactivity. However, our measurements suggest that the effect is small. Indeed, since the lifetimes of quasibound CH$^+$($^3\Pi$) molecules should be shorter than those of CD$^+$($^3\Pi$), one would expect to measure larger cross sections for reaction (2) than for reaction (1) due to contribution of quasibound states. But our merged-beams results shown in Fig. 4 and 5 do not display any significant isotope effects.

5.4 Comparison to capture models

The measured cross sections provide evidence that reactions (1) and (2) are barrierless exoergic reactions. Hence, it is interesting to compare the experimental results with the predictions of capture models, which are designed for such reactions. The simplest approach is the LGS model,[24,27] where the reactants are considered as structureless particles with isotropic charge distributions. Here, this approximates the C(^{3}P) dipole polarizability as an isotropic tensor and fails to account for its non-zero quadrupole moment. Hence, all electronic states that originate from C(^{3}P) + H$_2^+$($^2\Sigma_g^+$) are characterized at long range by the same attractive interaction potential corresponding to the charge-induced dipole interaction (note that induced interactions are always attractive). The resulting LGS capture cross section is written in atomic units as

$$\sigma_\alpha = \pi q \left(\frac{2\alpha}{E_r}\right)^{1/2}, \tag{35}$$

where q is the charge of the cation and $\alpha = 11.7$ bohr^3 is the mean static dipole polarizability of the ground-term C(^{3}P).[126]

Schuette and Gentry[40] employed an improved capture model that takes into account the anisotropic charge distribution of the C(^{3}P) and includes the effects of spin–orbit interactions on the interaction potentials.[45] In their model, the two main contributions to the long-range interaction potentials were accounted for, namely the charge-quadrupole electrostatic interaction and the charge-induced dipole interaction. Due to the anisotropy of the C(^{3}P) quadrupole moment and dipole polarizability, the various electronic states that originate from C(^{3}P) + H$_2^+$($^2\Sigma_g^+$) are characterized at long range by two distinct interaction potentials. The effect of spin–orbit interactions is to mix and split these interaction potentials. At very large

This journal is © the Owner Societies 2020

Phys. Chem. Chem. Phys., 2020, **22**, 27364–27384 | **27379**

ion–atom distances R, where the charge-quadrupole and charge-induced dipole interaction energies are smaller than the spin–orbit splittings, there are six interaction potentials that depend on the quantum numbers J and $|M_J|$, where J is the total angular momentum of the C(^{3}P$_{J=0,1,2}$) fine structure states and M_J its projection onto the ion–atom axis. With decreasing R, the charge-quadrupole and charge-induced dipole inter-action energies become larger than the spin–orbit splittings, and the $(J,|M_J|)$ potentials converge towards either one of two potentials that depend on the quantum number $|M_L|$, where M_L is the projection of the C(^{3}P) orbital angular momentum L onto the ion–atom axis.

The $|M_L|$ potentials correlate with the adiabatic PESs of CH$_2$$^+$ corresponding to a specific value of $\Lambda = |M_L|$ for collinear approach of the reactants ($C_{\infty v}$ symmetry), where Λ is the projection of the total electronic orbital angular momentum onto the ion–atom axis. The long-range potential for $|M_L| = 1$ is attractive and describes the long-range part of the $^2\Pi$ and $^4\Pi$ PESs, whereas that for $M_L = 0$ is repulsive and describes the long-range part of the $^2\Sigma^-$ and $^4\Sigma^-$ PESs. Since the long-range interactions are independent of the orientation of the reactants, the $|M_L|$ potentials also hold to describe the long-range part of the PESs of CH$_2$$^+$ for any configuration of C_s symmetry. At very large R, the spin–orbit couplings lead to $(J,|M_J|)$ potentials that are a mix of the $|M_L|$ potentials of Σ and Π character. For C(^{3}P) interacting with H$_2$$^+$($^2\Sigma_g^+$), the spin–orbit couplings are sufficiently small that the repulsive or attractive behavior of the $|M_L|$ potentials is preserved for the $(J,|M_J|)$ potentials at any value of R.[45]

Schuette and Gentry determined the capture cross sections $\sigma_{J,|M_J|}$ for each of the $(J,|M_J|)$ potentials, and the average cross section,

$$\sigma_{\Theta\alpha} = \frac{1}{\sum_J (2J+1)} \sum_J \sum_{M_J=-1}^{J} \sigma_{J,|M_J|}, \tag{36}$$

was reported for the $\sim$0.001–0.1 eV collision energy range.[40] The label $\sigma_{\Theta\alpha}$ is used to specify that both the C(^{3}P) quadrupole moment Θ and dipole polarizability α were accounted for to describe the long-range potentials. For collision energies below 0.1 eV, only the attractive potentials that correlate with the $^2\Pi$ and $^4\Pi$ PESs in $C_{\infty v}$ symmetry contribute to the reaction cross section.

The capture cross sections σ_α and $\sigma_{\Theta\alpha}$ are compared to the merged-beams cross sections of reactions (1) and (2) in Fig. 5. As can be seen, the two capture models yield reaction cross sections of similar magnitude. This is an unexpected result as the LGS model does not include the charge-quadrupole inter-action, which is the dominant contribution to the long-range interactions. For the present system, it appears that this lack is almost exactly counterbalanced by the LGS assumption that all electronic states emerging from C(^{3}P) + H$_2$$^+$($^2\Sigma_g^+$) contribute to the reaction due to the charge-induced dipole interaction. As for the energy dependence of $\sigma_{\Theta\alpha}$ shown in Fig. 5, it varies as $E_r^{-0.57}$, in better agreement with the behavior of the merged-beams cross sections than the $E_r^{-1/2}$ variation predicted by the

LGS model. However, both σ_α and $\sigma_{\Theta\alpha}$ are found to be larger than the experimental cross sections by a factor of $\sim$4 for $E_r < 0.1$ eV. This large discrepancy indicates that important features of the reaction are missing in the two capture models described above.

Taking into account the internal excitation of the parent cations in the experiment and the various electronic states that originate from the C(^{3}P) + H$_2$$^+$($^2\Sigma_g^+$) reactants, the ICS for reactions (1) and (2) can be written as

$$\sigma = \sum_v \sum_j \sum_i p_{\rm vib}(v) p_{\rm rot}(j) p_{\rm el}(i) \sigma(v,j,i), \tag{37}$$

where $p_{\rm vib}(v)$ and $p_{\rm rot}(j)$ are, respectively, the vibrational and rotational population distributions of H$_2$$^+$($v,j$) and D$_2$$^+$($v,j$) arising from the EII source (see Table 1); $p_{\rm el}(i)$ is the probability for the collision to initiate in the electronic state i; and $\sigma(v,j,i)$ is the reaction cross section for the electronic state i and a selected rovibrational state (v,j) of the cation molecules. Build-ing on the findings of Sections 3.1, 3.2, and 5.3, we make several assumptions about the reaction channels and reactant states that drive reactions (1) and (2) at low collision energy. In specific, we assume that: (a) the proton-transfer reaction proceeds only through the reaction channel (21), which involves the first two quartet states 1^{4}A$'$ and 1^{4}A$''$ of CH$_2$$^+$ that correlate with the $^4\Pi$ state in $C_{\infty v}$ symmetry; (b) only the H$_2$$^+$($v \leq 2$) and D$_2$$^+$($v \leq 3$) vibrational states contribute to the reaction; (c) all the populated rotational states of H$_2$$^+$($v \leq 2$) and D$_2$$^+$($v \leq 3$) contribute to the reaction; and (d) the reaction cross section is independent of the rovibrational state of the parent cations for H$_2$$^+$($v \leq 2$) and D$_2$$^+$($v \leq 3$). Introducing these assumptions into eqn (37) leads to the simplified expression

$$\sigma = p_{\rm vib} p_{\rm el}(^4\Pi) \sigma(^4\Pi), \tag{38}$$

where $p_{\rm vib} = \sum_{v=0}^{v_{\rm max}} p_{\rm vib}(v) \approx 0.50$ and 0.44 using the $p_{\rm vib}(v)$ values of Table 1 for H$_2$$^+$($v \leq 2$) and D$_2$$^+$($v \leq 3$), respectively; and $p_{\rm el}(^4\Pi) = 8/18$ is the probability for the collision to initiate in either one of the 1^{4}A$'$ and 1^{4}A$''$ states that drive reaction (21). The probability $p_{\rm el}(^4\Pi)$ can be determined by accounting for the degeneracy $g = g_{\rm spin} g_{\rm orbital}$ of each of the $^2\Sigma^-$, $^4\Sigma^-$, $^2\Pi$ and $^4\Pi$ electronic states that correlate with the C(^{3}P) + H$_2$$^+$($^2\Sigma_g^+$) reactants in $C_{\infty v}$ symmetry. Here we have $g_{\rm spin} = 2$ and 4 for the states of doublet and quartet spin multiplicity, respectively; and $g_{\rm orbital} = 1$ and 2 for the states of Σ and Π symmetry, respectively. Summing up the degeneracies of all states leads to a count of 18 states arising from C(^{3}P) + H$_2$$^+$($^2\Sigma_g^+$), of which 8 correspond to the $^4\Pi$ state, which splits into the 1^{4}A$'$ and 1^{4}A$''$ states in C_s symmetry.

The cross section $\sigma(^4\Pi)$ of eqn (38) corresponds to the average value that would be obtained from the 1^{4}A$'$ and 1^{4}A$''$ PESs that drive reaction (21). In the absence of PESs for these two quartet states, we can infer approximate values for $\sigma(^4\Pi)$ from the capture cross sections σ_α and $\sigma_{\Theta\alpha}$ defined by eqn (35) and (36), respectively. Since the LGS model assumes that all electronic states are characterized by the same long-range potential, the LGS cross section σ_α holds for any state arising from C(^{3}P) + H$_2$$^+$($^2\Sigma_g^+$). Thus, for the theoretical model outlined
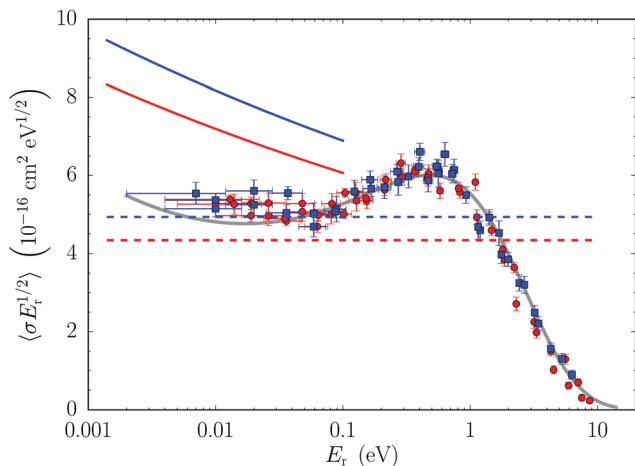
Fig. 7 Energy-weighted cross section $\langle \sigma E_{\mathrm{r}}^{1/2} \rangle$ as a function of the relative translational energy E_{r}. Results for reaction (1) are shown in blue and for reaction (2) in red. Our merged-beams results are shown by the data points with error bars. The gray solid line corresponds to 0.796 times the experimental results of Schuette and Gentry[40] for reaction (2). The dashed blue and red lines show the capture cross sections $\sigma'_{\alpha} E_{\mathrm{r}}^{1/2}$ corresponding to pure charge-induced dipole interactions. The solid blue and red lines show the capture cross sections $\sigma'_{\Theta\alpha} E_{\mathrm{r}}^{1/2}$ corresponding to charge-quadrupole and charge-induced dipole interactions and including the effects of spin–orbit interactions.[40,45] The capture cross sections shown here account only for reaction channel (21) and the contribution of the $H_2^+(v \le 2)$ and $D_2^+(v \le 3)$ states.

by eqn (38), we use $\sigma(^4\Pi) \approx \sigma_{\alpha}$. We label the ICS value resulting from this modified LGS model as σ'_{α}. The average capture cross section $\sigma_{\Theta\alpha}$ determined by Schuette and Gentry[40] accounts for the contribution of all attractive states that correlate with the $^2\Pi$ and $^4\Pi$ states in $C_{\infty v}$ symmetry. Since the theoretical model of eqn (38) assumes that only the quartet states lead to the formation of CH^+ molecules, and since the $^2\Pi$ and $^4\Pi$ states are characterized by the same long-range Π potential, we use $p_{\mathrm{el}}(^4\Pi)\sigma(^4\Pi) \approx (8/12)\sigma_{\Theta\alpha}$, where the ratio 8/12 stems from the probability to populate the quartet states for reactants approaching on the attractive Π potential. We label the ICS value resulting from this modified capture model as $\sigma'_{\Theta\alpha}$.

The merged-beams energy-weighted cross sections $\langle \sigma E_{\mathrm{r}}^{1/2} \rangle$ for reactions (1) and (2) are compared in Fig. 7 to the theoretical results obtained for σ'_{α} and $\sigma'_{\Theta\alpha}$. Owing to their underlying assumptions, the modified capture models are primarily relevant for describing the low-energy behavior of the reaction. For $E_{\mathrm{r}} < 0.1$ eV the magnitude of $\sigma'_{\alpha} E_{\mathrm{r}}^{1/2}$ from the modified LGS model is close to that of the experimental results. However, the model does not correctly reproduce the energy dependence of the experimental results. In addition, for most of the collision energies probed in the experiment, the merged-beams results are larger than predicted by the modified LGS model. This points to short-comings in the theoretical model, as capture models assume that a reaction proceeds with unit probability. Accordingly, the modified LGS model should provide an upper limit to the experimental cross sections. We attribute the observed discrepancies in the present case to the lack of the charge-quadrupole contribution to the long-range interactions in the LGS model.

The modified capture model of Schuette and Gentry[40] incorporates both the charge-induced dipole and charge-quadrupole contributions to the long-range interactions. As can be seen in Fig. 7, the resulting $\sigma'_{\Theta\alpha} E_{\mathrm{r}}^{1/2}$ more properly describes the low energy behavior of the merged-beams results than do the modified LGS results. The results of the modified model of Schuette and Gentry also show the expected capture model behavior, as the cross sections are larger than the experimental results by a factor of ~ 1.5 and ~ 1.3 for reactions (1) and (2), respectively. These discrepancies are much smaller than the factor of ~ 4 of discrepancy obtained between the unmodified capture models and the measurements (see Fig. 5). This improvement supports our hypotheses that the proton-transfer reaction proceeds primarily through reaction (21) at low collision energy, and that only a limited range of reactant states, $H_2^+(v \le 2)$ and $D_2^+(v \le 3)$, lead to the formation of stable $CH^+(^3\Pi)$ and $CD^+(^3\Pi)$ products. The remaining discrepancies between $\sigma'_{\Theta\alpha} E_{\mathrm{r}}^{1/2}$ and the experimental results may be explained by a non-negligible contribution of the competing DCT process (29), which could reduce the reaction probability for the $H_2^+(v \le 2)$ and $D_2^+(v \le 3)$ states. If that is the case, then the larger discrepancies observed for reaction (1) compared to reaction (2) would indicate that the DCT process is more efficient for the $H_2^+(v \le 2)$ states than for the $D_2^+(v \le 3)$ states, due to an increasing tunneling probability for the lighter isotope. This could potentially also explain the lack of an intermolecular isotope effect seen in the experimental results.

6 Summary

We have measured the dynamics of reactions (1) and (2) using a beam of ground term $C(^3P)$ with statistically populated fine-structure levels and beams of H_2^+ and D_2^+ with well known vibrational and rotational distributions. Our results provide evidence that the reactions are barrierless and exoergic. They also indicate the apparent absence of an intermolecular isotope effect. Comparing our results to those of Schuette and Gentry[40] for reaction (2), we find good agreement. Our findings indicate that their CT-generated neutral C beam was essentially free of metastable levels, a systematic uncertainty in their results that they were unable to rule out and that hindered the comparison of their results with theory. That the cross section findings of both groups lie a factor of ~ 4 below capture model predictions indicates shortcomings in the models. We have also carried out a complementary theoretical study of the CH_2^+ electronic system in the reactant and product channels in order to help clarify the likely reaction mechanisms. We found that the reactions are most likely to proceed adiabatically through the $1^4A'$ and $1^4A''$ states of CH_2^+ leading to formation of $CH^+(^3\Pi)$ and $CD^+(^3\Pi)$ molecules via reaction (21). We also found that at low collision energies only $H_2^+(v \le 2)$ and $D_2^+(v \le 3)$ are likely to contribute to the reaction, due to the onset of DCT for higher vibrational levels. Incorporating these assumptions into capture models brings them into better agreement with the experimental results, though significant difference still remain

This journal is © the Owner Societies 2020

Phys. Chem. Chem. Phys., 2020, **22**, 27364–27384 | **27381**

that indicate the need for more sophisticated theoretical treatments. Our findings provide important guidance for future QCT and QM treatments of this reaction.

Conflicts of interest

There are no conflicts of interest.

Acknowledgements

References

1 D. McElroy, C. Walsh, A. J. Markwick, M. A. Cordiner, K. Smith and T. J. Millar, *Astron. Astrophys.*, 2013, **550**, A36.

2 V. Wakelam, J.-C. Loison, E. Herbst, B. Pavone, A. Bergeat, K. Béroff, M. Chabot, A. Faure, D. Galli, W. D. Geppert, D. Gerlich, P. Gratier, N. Harada, K. M. Hickson, P. Honvault, S. J. Klippenstein, S. D. Le Picard, G. Nyman, M. Ruaud, S. Schlemmer, I. R. Sims, D. Talbi, J. Tennyson and R. Wester, *Astrophys. J., Suppl. Ser.*, 2015, **217**, 20.

3 J. Prager, U. Riedel and J. Warnatz, *Proc. Combust. Inst.*, 2007, **31**, 1129–1137.

4 D. Kim, F. Rizzi, K. W. Cheng, J. Han, F. Bisetti and O. M. Knio, *Combust. Flame*, 2015, **162**, 2904–2915.

5 J. G. Wang and P. C. Stancil, *Phys. Scr.*, 2002, **T96**, 72–85.

6 Y. H. Kim, J. L. Fox, J. H. Black and J. I. Moses, *J. Geophys. Res.: Space Phys.*, 2014, **119**, 384–395.

7 V. Vuitton, O. Dutuit, M. A. Smith and N. Balucani, in *Chemistry of Titan's atmosphere*, ed. I. Müller-Wodarg, C. A. Griffith, E. Lellouch and T. E. Cravens, Cambridge University Press, Cambridge, U.K., 2014, pp. 224–284.

8 N. S. Shuman, D. E. Hunton and A. A. Viggiano, *Chem. Rev.*, 2015, **115**, 4542–4570.

9 K. Hassouni, F. Silva and A. Gicquel, *J. Phys. D: Appl. Phys.*, 2010, **43**, 153001.

10 Y. Sakiyama, D. B. Graves, H.-W. Chang, T. Shimizu and G. E. Morfill, *J. Phys. D: Appl. Phys.*, 2012, **45**, 425201.

11 V. G. Anicich, *J. Phys. Chem. Ref. Data*, 1993, **22**, 1469–1569.

12 S. C. Althorpe and D. C. Clary, *Annu. Rev. Phys. Chem.*, 2003, **54**, 493–529.

13 J. M. Bowman, G. Czakó and B. Fu, *Phys. Chem. Chem. Phys.*, 2011, **13**, 8094–8111.

14 A. O'Connor, X. Urbain, J. Stützel, K. A. Miller, N. de Ruette, M. Garrido and D. W. Savin, *Astrophys. J., Suppl. Ser.*, 2015, **219**, 6.

15 P. Gamallo, S. Akpinar, P. Defazio and C. Petrongolo, *J. Phys. Chem. A*, 2014, **118**, 6451–6456.

16 P. Gamallo, P. Defazio, M. González, M. Paniagua and C. Petrongolo, *Phys. Chem. Chem. Phys.*, 2015, **17**, 23392–23402.

17 R. Martínez, M. Paniagua, J. Mayneris-Perxachs, P. Gamallo and M. González, *Phys. Chem. Chem. Phys.*, 2017, **19**, 3857–3868.

18 A.-J. Zhang, K.-L. Zang, J.-F. Jia, H.-S. Wu, Yi-Wang and G.-J. Zhao, *Chem. Phys. Lett.*, 2017, **676**, 77–81.

19 Y. Zhang, E. Cao, S. Gao, X. Huang, Q. Meng and Y. Song, *Int. J. Quantum Chem.*, 2017, **117**, 25343.

20 N. de Ruette, K. A. Miller, A. P. O'Connor, X. Urbain, C. F. Buzard, S. Vissapragada and D. W. Savin, *Astrophys. J.*, 2016, **816**, 31.

21 P. M. Hillenbrand, K. P. Bowen, J. Liévin, X. Urbain and D. W. Savin, *Astrophys. J.*, 2019, **877**, 38.

22 L. M. Raff and D. L. Thompson, in *The Classical Trajectory Approach to Reactive Scattering*, ed. M. Baer, CRC, Boca Raton, 1985, vol. 3, pp. 1–121.

23 J. C. Light and J. Lin, *J. Chem. Phys.*, 1965, **43**, 3209–3219.

24 R. D. Levine, *Molecular Reaction Dynamics*, Cambridge University Press, Cambridge, 2005.

25 D. C. Clary, *Annu. Rev. Phys. Chem.*, 1990, **41**, 61–90.

26 D. Zhang and S. Willitsch, in *Cold Ion Chemistry*, ed. O. Dulieu and A. Osterwalder, The Royal Society of Chemistry, 2018, pp. 496–536.

27 G. Gioumousis and D. P. Stevenson, *J. Chem. Phys.*, 1958, **29**, 294–299.

28 A. Fernàndez-Ramos, J. A. Miller, S. J. Klippenstein and D. G. Truhlar, *Chem. Rev.*, 2006, **106**, 4518–4584.

29 Y. V. Suleimanov, F. J. Aoiz and H. Guo, *J. Phys. Chem. A*, 2016, **120**, 8488–8502.

30 D. De Fazio, M. de Castro-Vitores, A. Aguado, V. Aquilanti and S. Cavalli, *J. Chem. Phys.*, 2012, **137**, 244306.

31 M. Hernández Vera, R. Wester and F. A. Gianturco, *J. Phys. B: At., Mol. Opt. Phys.*, 2018, **51**, 014004.

32 D. Koner, J. C. San Vicente Veliz, A. van der Avoird and M. Meuwly, *Phys. Chem. Chem. Phys.*, 2019, **21**, 24976–24983.

33 E. Aslan, N. Bulut, J. F. Castillo, L. Bañares, O. Roncero and F. J. Aoiz, *J. Phys. Chem. A*, 2012, **116**, 132–138.

34 X. He, S. Lv, T. Hayat and K. Han, *J. Phys. Chem. A*, 2016, **120**, 2459–2470.

35 P. Gamallo, R. Martnez, J. D. Sierra and M. González, *Phys. Chem. Chem. Phys.*, 2014, **16**, 6641.

36 C.-X. Yao and P.-Y. Zhang, *J. Phys. Chem. A*, 2014, **118**, 5076–5082.

37 H. Wu, C.-X. Yao, X.-H. He and P.-Y. Zhang, *J. Chem. Phys.*, 2016, **144**, 184301.

38 E. Tans, E. Ylmaz and E. Karabulut, *Can. J. Phys.*, 2018, **96**, 1395–1403.

39 M. Hu, W. Xu, X. Liu, R. Tan and H. Li, *J. Chem. Phys.*, 2013, **138**, 174305.

40 G. F. Schuette and W. R. Gentry, *J. Chem. Phys.*, 1983, **78**, 1777–1785.

41 D. J. McClure, C. H. Douglass and W. R. Gentry, *J. Chem. Phys.*, 1977, **66**, 2079–2093.

42 D. J. McClure, C. H. Douglass and W. R. Gentry, *J. Chem. Phys.*, 1977, **67**, 374.

43 D. J. McClure, C. H. Douglass and W. R. Gentry, *J. Chem. Phys.*, 1977, **67**, 2362–2370.

44 G. F. Schuette and W. R. Gentry, *J. Chem. Phys.*, 1983, **78**, 1786–1794.

45 W. R. Gentry and C. F. Giese, *J. Chem. Phys.*, 1977, **67**, 2355–2361.

46 X. N. Tang, H. Xu, T. Zhang, Y. Hou, C. Chang, C. Y. Ng, Y. Chiu, R. A. Dressler and D. J. Levandier, *J. Chem. Phys.*, 2005, **122**, 164301.

47 B. Xiong, Y.-C. Chang and C.-Y. Ng, *Phys. Chem. Chem. Phys.*, 2017, **19**, 18619–18627.

48 J. A. Rutherford and D. A. Vroom, *J. Chem. Phys.*, 1973, **58**, 4076–4079.

49 R. H. Neynaber and G. D. Magnuson, *J. Chem. Phys.*, 1973, **59**, 825–831.

50 T. Turner, Y. T. Lee and O. Dutuit, *J. Chem. Phys.*, 1984, **81**, 3475–3481.

51 T. Zhang, X. M. Qian, X. N. Tang, C. Y. Ng, Y. Chiu, D. J. Levandier, J. S. Miller and R. A. Dressler, *J. Chem. Phys.*, 2003, **119**, 10175–10185.

52 R. A. Dressler, Y. Chiu, D. J. Levandier, X. N. Tang, Y. Hou, C. Chang, C. Houchins, H. Xu and C.-Y. Ng, *J. Chem. Phys.*, 2006, **125**, 132306.

53 B. Xiong, Y.-C. Chang and C.-Y. Ng, *Phys. Chem. Chem. Phys.*, 2017, **19**, 29057–29067.

54 H. Song, A. Li, H. Guo, Y. Xu, B. Xiong, Y.-C. Chang and C. Y. Ng, *Phys. Chem. Chem. Phys.*, 2016, **18**, 22509–22515.

55 Y. Xu, B. Xiong, Y. C. Chang and C. Y. Ng, *Phys. Chem. Chem. Phys.*, 2017, **19**, 8694–8705.

56 Y. Xu, B. Xiong, Y.-C. Chang, Y. Pan, P. K. Lo, K. C. Lau and C. Y. Ng, *Phys. Chem. Chem. Phys.*, 2017, **19**, 9778–9789.

57 Y. Xu, B. Xiong, Y. Chung Chang and C.-Y. Ng, *Astrophys. J.*, 2018, **861**, 17.

58 Y. Xu, Y. Chung Chang, Z. Lu and C. Y. Ng, *Astrophys. J.*, 2013, **769**, 72.

59 Y. Xu, B. Xiong, Y. C. Chang and C.-Y. Ng, *J. Phys. Chem. A*, 2018, **122**, 6491–6499.

60 F. von Busch and G. H. Dunn, *Phys. Rev. A: At., Mol., Opt. Phys.*, 1972, **5**, 1726–1743.

61 D. de Bruijn, J. Neuteboom and J. Los, *Chem. Phys.*, 1984, **85**, 233–251.

62 S. Krohn, Z. Amitay, A. Baer, D. Zajfman, M. Lange, L. Knoll, J. Levin, D. Schwalm, R. Wester and A. Wolf, *Phys. Rev. A: At., Mol., Opt. Phys.*, 2000, **62**, 032713.

63 D. Zajfman, S. Krohn, M. Lange, H. Kreckel, L. Lammich, D. Strasser, D. Schwalm, X. Urbain and A. Wolf, *Nucl. Instrum. Methods Phys. Res., Sect. B*, 2003, **205**, 360–366.

64 N. de Ruette, PhD thesis, Université catholique de Louvain, Louvain-la-Neuve, Belgium, 2007.

65 A. P. O'Connor, F. Grussie, H. Kreckel, H. Bruhns, K. A. Miller, N. de Ruette, J. Stützel, D. W. Savin, T. P. Koening and X. Urbain, *Rev. Sci. Instrum.*, 2015, **86**, 113806.

66 E. Hugo, O. Asvany and S. Schlemmer, *J. Chem. Phys.*, 2009, **130**, 164302.

67 K. P. Huber and G. Herzberg, *Molcular Spectra and Molecular Structure. IV. Constants of Diatomic Molecules*, Van Nostrand Reinhold, New York, 1979.

68 M. Scheer, R. C. Bilodeau, C. A. Brodie and H. K. Haugen, *Phys. Rev. A: At., Mol., Opt. Phys.*, 1998, **58**, 2844–2856.

69 H. Bruhns, H. Kreckel, K. A. Miller, X. Urbain and D. W. Savin, *Phys. Rev. A: At., Mol., Opt. Phys.*, 2010, **82**, 042708.

70 A. Zanchet, B. Godard, N. Bulut, O. Roncero, P. Halvick and J. Cernicharo, *Astrophys. J.*, 2013, **766**, 80.

71 D. Herráaez-Aguilar, P. G. Jambrina, M. Menéndez, J. Aldegunde, R. Warmbier and F. J. Aoiz, *Phys. Chem. Chem. Phys.*, 2014, **16**, 24800–24812.

72 J. Guo, A. J. Zhang, Y. Zhou, J. Y. Liu, J. F. Jia and H. S. Wu, *Chem. Phys. Lett.*, 2017, **689**, 121–127.

73 Y. Q. Li, P. Y. Zhang and K. L. Han, *J. Chem. Phys.*, 2015, **142**, 124302.

74 G. Werfelli, P. Halvick, P. Honvault, B. Kerkeni and T. Stoecklin, *J. Chem. Phys.*, 2015, **143**, 114304.

75 P. Sundaram, V. Manivannan and R. Padmanaban, *Phys. Chem. Chem. Phys.*, 2017, **19**, 20172–20187.

76 L. Guo, H. Ma, L. Zhang, Y. Song and Y. Li, *RSC Adv.*, 2018, **8**, 13635–13642.

77 R. Jaquet and V. Staemmler, *Chem. Phys.*, 1982, **68**, 479–489.

78 W. Reuter and S. D. Peyerimhoff, *Chem. Phys.*, 1992, **160**, 11–24.

79 M. Bonfanti, G. F. Tantardini and R. Martinazzo, *J. Phys. Chem. A*, 2014, **118**, 6595–6603.

80 N. R. Brinkmann, N. A. Richardson, S. S. Wesolowski, Y. Yamaguchi and H. F. Schaefer III, *Chem. Phys. Lett.*, 2002, **352**, 505–510.

81 C. Galloy and J. Lorquet, *Chem. Phys.*, 1978, **30**, 169–176.

82 S. Sakai, S. Kato, K. Morokuma and I. Kusunoki, *J. Chem. Phys.*, 1981, **75**, 5398–5409.

83 A. Kramida, Y. Ralchenko, J. Reader and NIST ASD Team, *NIST Atomic Spectra Database (version 5.6.1)*, National Institute of Standards and Technology, Gaithersburg, MD, 2018, https://physics.nist.gov/asd.

84 A. Ishikawa, H. Nakashima and H. Nakatsuji, *Chem. Phys.*, 2012, **401**, 62–72.

85 M. Zachwieja, *J. Mol. Spectrosc.*, 1995, **170**, 285–309.

86 A. Kalemos, A. Mavridis and A. Metropoulos, *J. Chem. Phys.*, 1999, **111**, 9536–9548.

87 T. Nelis, J. M. Brown and K. M. Evenson, *J. Chem. Phys.*, 1990, **92**, 4067–4076.

88 S. Yu, B. J. Drouin, J. C. Pearson and T. Amano, *J. Mol. Spectrosc.*, 2018, **350**, 30–36.

89 U. Hechtfischer, C. J. Williams, M. Lange, J. Linkemann, D. Schwalm, R. Wester, A. Wolf and D. Zajfman, *J. Chem. Phys.*, 2002, **117**, 8754–8777.

90 U. Hechtfischer, J. Rostas, M. Lange, J. Linkemann, D. Schwalm, R. Wester, A. Wolf and D. Zajfman, *J. Chem. Phys.*, 2007, **127**, 204304.

91 Z. Biglari, A. Shayesteh and A. Maghari, *Comput. Theor. Chem.*, 2014, **1047**, 22–29.

92 H. Helm, P. C. Cosby, M. M. Graff and J. T. Moseley, *Phys. Rev. A: At., Mol., Opt. Phys.*, 1982, **25**, 304–321.

93 R. Hakalla, R. Kepa, W. Szajna and M. Zachwieja, *Eur. Phys. J. D*, 2006, **38**, 481–488.

94 J.-B. Song and E. A. Gislason, *Chem. Phys.*, 2003, **293**, 231–237.

95 B. H. Mahan, *Acc. Chem. Res.*, 1975, **8**, 55–61.

96 M. Sizun, J.-B. Song and E. A. Gislason, *J. Chem. Phys.*, 1998, **109**, 4815–4822.

97 S. Chapman and R. K. Preston, *J. Chem. Phys.*, 1974, **60**, 650–659.

98 R. K. Preston, D. L. Thompson and D. R. McLaughlin, *J. Chem. Phys.*, 1978, **68**, 13–21.

99 P. Kuntz, J. Kendrick and W. Whitton, *Chem. Phys.*, 1979, **38**, 147–160.

100 V. Sidis, *J. Phys. Chem.*, 1989, **93**, 8128–8138.

101 F. A. Houle, S. L. Anderson, D. Gerlich, T. Turner and Y. T. Lee, *J. Chem. Phys.*, 1982, **77**, 748–755.

102 S. Chapman, *J. Chem. Phys.*, 1985, **82**, 4033–4043.

103 C.-L. Liao, R. Xu, G. D. Flesch, M. Baer and C. Y. Ng, *J. Chem. Phys.*, 1990, **93**, 4818–4831.

104 H.-J. Werner and P. J. Knowles, *J. Chem. Phys.*, 1988, **89**, 5803–5814.

105 P. J. Knowles and H.-J. Werner, *Chem. Phys. Lett.*, 1988, **145**, 514–522.

106 S. R. Langhoff and E. R. Davidson, *Int. J. Quantum Chem.*, 1974, **8**, 61–72.

107 H.-J. Werner and P. J. Knowles, *J. Chem. Phys.*, 1985, **82**, 5053–5063.

108 P. J. Knowles and H.-J. Werner, *Chem. Phys. Lett.*, 1985, **115**, 259–267.

109 T. H. Dunning, *J. Chem. Phys.*, 1989, **90**, 1007–1023.

110 R. A. Kendall, T. H. Dunning and R. J. Harrison, *J. Chem. Phys.*, 1992, **96**, 6796–6806.

111 H.-J. Werner, P. J. Knowles, G. Knizia, F. R. Manby and M. Schütz, *et al.*, *MOLPRO, version 2012.1, a package of ab initio programs*, 2012, see http://www.molpro.net.

112 C. C. Marston and G. G. Balint-Kurti, *J. Chem. Phys.*, 1989, **91**, 3571–3576.

113 I. Kusunoki and C. Ottinger, *J. Chem. Phys.*, 1982, **76**, 1845–1852.

114 T. Michaelsen, B. Bastian, E. Carrascosa, J. Meyer, D. H. Parker and R. Wester, *J. Chem. Phys.*, 2017, **147**, 013940.

115 F. Aguillon, *J. Chem. Phys.*, 1998, **109**, 560–571.

116 D. De Fazio, A. Aguado and C. Petrongolo, *Fron. Chem.*, 2019, **7**, 249.

117 C. H. Douglass, G. Ringer and W. R. Gentry, *J. Chem. Phys.*, 1982, **76**, 2423–2429.

118 I. Savić, I. Cermák and D. Gerlich, *Int. J. Mass Spectrom.*, 2005, **240**, 139–147.

119 T. Albertsson, D. A. Semenov, A. I. Vasyunin, T. Henning and E. Herbst, *Astrophys. J., Suppl. Ser.*, 2013, **207**, 27.

120 C. Ceccarelli, P. Caselli, D. Bockelée-Morvan, O. Mousis, S. Pizzarello, F. Robert and D. Semenov, *Protostars and Planets VI*, 2014, pp. 859–882.

121 T. J. Millar, *Plasma Sources Sci. Technol.*, 2015, **24**, 043001.

122 O. Sipilä, P. Caselli and J. Harju, *Astron. Astrophys.*, 2015, **578**, A55.

123 S. Kong, P. Caselli, J. C. Tan, V. Wakelam and O. Sipilä, *Astrophys. J.*, 2015, **804**, 98.

124 L. Majumdar, P. Gratier, M. Ruaud, V. Wakelam, C. Vastel, O. Sipilä, F. Hersant, A. Dutrey and S. Guilloteau, *Mon. Not. R. Astron. Soc.*, 2017, **466**, 4470–4479.

125 Y. Aikawa, K. Furuya, U. Hincelin and E. Herbst, *Astrophys. J.*, 2018, **855**, 119.

126 C. Thierfelder, B. Assadollahzadeh, P. Schwerdtfeger, S. Schäfer and R. Schäfer, *Phys. Rev. A: At., Mol., Opt. Phys.*, 2008, **78**, 052506.

27384 | *Phys. Chem. Chem. Phys.*, 2020, **22**, 27364–27384

This journal is © the Owner Societies 2020